國立臺灣大學理學院應用物理研究所

碩士論文

Graduate Institute of Applied Physics

College of Science

National Taiwan University

Master Thesis

雷射頻率穩定於高精密度腔體用於銫原子的雷德堡激發

Laser Frequency Stabilization to a High-Finesse Cavity for Cesium Rydberg Excitations

李芳瑜

Fang-Yu Lee

指導教授: 林俊達 博士、陳應誠 博士

Advisor: Guin-Dar Lin, Ph.D., Ying-Cheng Chen, Ph.D.

中華民國 112 年 8 月

August, 2023

doi:10.6342/NTU202302912

國立臺灣大學碩士學位論文
口試委員會審定書
MASTER'S THESIS ACCEPTANCE CERTIFICATE
NATIONAL TAIWAN UNIVERSITY

雷射頻率穩定於高精密度腔體用於銫原子的雷德堡激發

Laser frequency stabilization to a high-finesse cavity for cesium Rydberg excitations

本論文係李芳瑜君 (R10245002) 在國立臺灣大學應用物理學研究所完成之碩士學位論文，於民國 112 年 7 月 21 日承下列考試委員審查通過及口試及格，特此證明。

The undersigned, appointed by the Graduate Institute of Applied Physics on 21 July 2023 have examined a Master's thesis entitled above presented by Lee, Fang-Yu (R10245002) candidate and hereby certify that it is worthy of acceptance.

口試委員 Oral examination committee:

林俊達 陳應誠 陳柏佑

（指導教授 Advisor）

劉扬銘

系主任/所長 Director: 張寶棣

doi:10.6342/NTU202302912

doi:10.6342/NTU202302912

致謝

加入量子光學實驗室是從大學暑期實習開始，在這遇見了很多對物理和研究抱有熱情的強者，便讓我興起了碩士也想這裡結束的念頭，於是再次不自量力的加入這間實驗室。

最感謝的是我在中研院原分所的指導老師陳應誠博士，讓我在搭建穩頻雷射的同時也學習了關於量子計算的知識，給了我很多實驗、報告上的建議及幫助，還有提供各種參加學術研討會的機會，抱歉在您充滿壓力的時候，不是一個能讓您省心的學生，謝謝您的指導以及各種經驗的分享，我會記得您總是笑著說研究好痛苦卻不減熱忱的模樣。接著也很感謝林俊達博士，總是及時提供我需要的幫助，讓我能在原分所專心的學習。還有口試委員劉怡維博士、陳姿伶博士給我的修改意見，幫助我讓論文內容更完整。

再來是 Lab330 的大家，謝謝在暑期實習以及碩班剛進實驗室帶領我給我最多幫助的蔡秉儒學長，以及到德國還遠端陪我解決問題的蕭雅棻學姐，很開心兩年後再次進到實驗室依舊有你們熟悉的鬥嘴。也很感謝彩妮學姐無論實驗、理論、報告或是生活上給我的各種幫助，總是溫柔地給我鼓勵。也謝謝于誌學長、奕嘉在我忙碌的時候幫我照顧系統，和排版小天才顏丞的幫忙，有你們真的幫了我很多。再來，謝謝翊亘、東駿的餵食，雖然老是鬥嘴但我會記得你們貼心的模樣。

感謝一直以來我的朋友們在這陌生城市給的陪伴，意識到自己的平凡和那些迷茫沮喪的時刻，給予我的安慰和幫助，都讓我好慶幸有你們。無法習慣台北的雨天，你們卻始終是我能躲雨的地方，悲傷有你們接著，而我更珍惜你們帶給我的快樂。

最後感謝我的父親、母親和弟弟在碩士班給我的所有支持，讓我不需要為了生活奔波。可能到了現在還是沒能成為不讓你們擔心的孩子，卻依然有你們足夠的體諒和無私的付出作為我可靠的避風港，我真的很幸福。

也謝謝那些無法逐一唱名卻幫助過我的所有人，你們的每個幫忙都很重要，我會帶著這兩年所有美好的回憶，成為我繼續前進的動力！

doi:10.6342/NTU202302912

doi:10.6342/NTU202302912

摘要

將中性原子激發到雷德堡態是實現量子計算的具潛力的眾多平台之一。因為雷德堡態強偶極-偶極相互作用，有效範圍可達數微米，並且可以由雷射控制的此交互作用，因此能夠個別單獨對每個量子位進行操作，來實現快速控制的量子閘。由於雷德堡態的長生命期，其自然線寬相當窄，僅在亞千赫茲的範圍內。因此，我們需要一台亞千赫茲、線寬窄且能夠精確鎖定頻率的雷射來實現高保真度和長相干時間的雙量子邏輯閘。我們使用 Pound-Drever-Hall 技術將 1039nm 和 918nm 波長的外腔二極體雷射器精確鎖定到一個與超低膨脹玻璃組成的高精度法布里-珀羅腔。1039nm 和 459nm 雷射器均用於激發銫原子至雷德堡態。459nm 雷射是由 918nm 雷射通過二倍頻晶體產生的。得到 1039 (918) nm 雷射的反饋頻寬高達 760kHz（1MHz）。另外，分析光通過共振腔體的強度擾動，我們估計在 40 毫秒的時間內，頻率的擾動範圍為 350Hz（621Hz）。這說明我們成功地抑制了雷射的相位噪聲。此外，我們利用穿透共振腔的穩頻雷射進行光功率放大，窄線寬的共振腔有效防止伺服凸點成為額外的噪聲源。最後，為了確定腔體的零交叉溫度，我們採用無都普勒飽和光譜技術量測零交叉溫度，並在此溫度附近觀察約 50 天，平均每天頻率漂移 7kHz，這使我們能夠根據觀察到的結果校正雷射的長期頻率頻移，並使用此雷射系統將原子激發到不同雷德堡態。

關鍵字：雷射相位噪音、雷射穩頻、雷德堡態、Pound-Drever-Hall 技術、飽和吸收光譜

doi:10.6342/NTU202302912

doi:10.6342/NTU202302912

Abstract

Neutral atoms excited to Rydberg states are one potential platform to realize quantum computing. The laser-controllable, strong dipole-dipole interactions which are effective at several micrometer range allow the implementation of fast and individual-addressable quantum gates. Nevertheless, owing to the long lifetime of Rydberg states, the natural linewidth is at the sub-kilohertz level. This demands the use of a sub-kHz, narrow linewidth laser that is tightly locked to achieve two-qubit gates with high fidelity and long coherence time. We lock an external-cavity diode laser (ECDL) at both 1039nm and 918nm wavelengths to a high finesse Fabry-Pérot cavity spaced with an ultra-low expansion glass (ULE) using the Pound-Drever-Hall (PDH) technique. Furthermore, the 459nm laser is generated by passing the 918nm laser through a second harmonic generation crystal, resulting in frequency doubling. Both the 1039nm and 459nm lasers are utilized as excitation lasers to drive cesium atoms to Rydberg states. The feedback bandwidth of the 1039nm (918nm) laser is as high as 760kHz (1MHz), allowing for precise control of the

doi:10.6342/NTU202302912

laser frequency. By analyzing the fluctuations in the transmitted light through the cavity, we estimate a frequency disturbance of 350Hz (621Hz) within a 40ms time interval, demonstrating the effective suppression of laser phase noise. Furthermore, we utilize the transmitted light through the cavity to amplify the optical power, effectively preventing servo bumps from becoming additional sources of noise. To determine the zero-crossing temperature of the cavity, we utilize Doppler-free saturation spectroscopy to accurately measure the frequency drift. The cavity is set near the zero-crossing temperature, and over a period of 50 days, we observe an average frequency drift of 7kHz per day. Using trap-loss spectroscopy, we have excited atoms to Rydberg states with this laser system.

Keywords: Laser phase noise, Laser frequency stabilization, Rydberg states, Pound-Drever-Hall technique, Doppler-free saturation spectroscopy

doi:10.6342/NTU202302912

Contents

doi:10.6342/NTU202302912

doi:10.6342/NTU202302912

doi:10.6342/NTU202302912

doi:10.6342/NTU202302912

List of Figures

doi:10.6342/NTU202302912

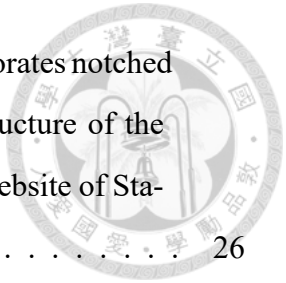

doi:10.6342/NTU202302912

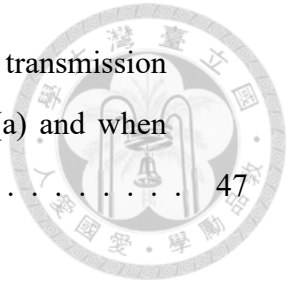

doi:10.6342/NTU202302912

doi:10.6342/NTU202302912

doi:10.6342/NTU202302912

doi:10.6342/NTU202302912

List of Tables

doi:10.6342/NTU202302912

doi:10.6342/NTU202302912

Chapter 1

Introduction

Neutral atoms excited to Rydberg states offer great potential as a platform for realizing quantum computing, and several research teams have already published their work on quantum gate and algorithm operations using Rydberg atoms [1][2]. However, achieving long coherence times and high fidelity in quantum operations with Rydberg atoms is a challenging task, and one significant obstacle is the phase noise of the lasers used in the Rydberg excitation. Laser phase noise introduces fluctuations in frequencies, leading to errors in quantum operations.

	Lifetime	Linewidth
$7P_{1/2}$	$\sim$ 150ns	$\sim$ 1MHz
$81S_{1/2}$	$\sim$200μs	$\sim$ 0.8kHz

Table 1.1: The lifetime of cesium atoms in our system at the intermediate state and Rydberg state.

In this chapter, we first explore the advantages of Rydberg atoms in quantum information processing and discuss their unique properties that make them a promising candidate for this purpose. Additionally, we discuss the implementation of two-qubit gates using Rydberg atoms, showing their potential for advancing quantum computing applications. Furthermore, we will emphasize the significance of laser phase noise in achieving long

doi:10.6342/NTU202302912

coherence times and high fidelity in quantum operations. We investigate the sources of laser phase noise and quantify it by analyzing laser linewidth and stability.

1.1 Rydberg Atoms in Quantum Information Processing

Rydberg atoms are atoms that have been excited to high principal quantum numbers n, resulting in a strong dipole moment that significantly influences their dipole-dipole interactions, which are proportional to n^4.The remarkable advantage of Rydberg atoms lies in their ability to precisely control the interactions between them, with the ability to turn these interactions on and off over a wide range, exhibiting a contrast of up to 12 orders of magnitude [3]. This precise control enables the manipulation of quantum bits with high precision. In addition, Rydberg atoms offer the ability to control entanglement between any two atoms by conveniently manipulating the distances between them using techniques like tweezers. Moreover, the long radiative lifetimes of Rydberg states, lasting over 100 microseconds, provide a long timescale for quantum gate operations in the microsecond range. These distinctive features make Rydberg atoms highly promising for applications in quantum information processing (QIP).

1.2 Implementation of Two-Qubit Quantum Gates

Using Rydberg blockade to implement a two-qubit gate is fundamental and crucial to quantum information processing. As shown in Fig. 1.1, in this implementation, initially, two atoms are in the state $|01\rangle$, where the control atom is not excited to the Rydberg state, while the target atom receives a 2π pulse, resulting in a π phase shift.

doi:10.6342/NTU202302912

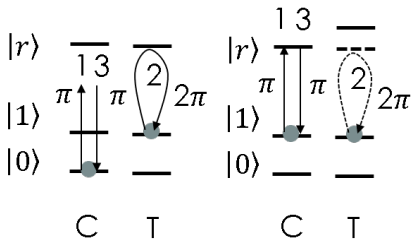

Figure 1.1: Operation of a controlled phase gate using Rydberg blockade.

When two atoms are initially in the state $|11\rangle$, the Rydberg blockade effect arises due to the significant interaction between Rydberg states compared to the excitation Rabi frequency. This leads to the blocking of excitation for the target atom, enabling the successful implementation of the controlled-Z gate, commonly referred to as the CZ gate. The evolution matrix in the computational basis $|00\rangle$,$|01\rangle$,$|10\rangle$,$|11\rangle$ is

$$CZ = \begin{pmatrix} 1 & 0 & 0 & 0 \\ 0 & -1 & 0 & 0 \\ 0 & 0 & -1 & 0 \\ 0 & 0 & 0 & -1 \end{pmatrix}. \tag{1.1}$$

The computational basis states are transformed by the unitary CZ gate as follows:

$$|q_1 q_2\rangle \rightarrow |q_1 q_2\rangle \phi_{q_1 q_2}. \tag{1.2}$$

Here, qubit 1 and qubit 2, denoted by q_1 and q_2 respectively, can each take the states 0 or 1. The CZ gate has a phase requirement given by:

$$\phi_{00} - \phi_{01} - \phi_{10} + \phi_{11} = \pm\pi. \tag{1.3}$$

This condition ensures that the CZ gate introduces the correct phase shift between different computational basis states, essential for performing quantum computations.

doi:10.6342/NTU202302912

The application of the Hadamard gate before and after the CZ gate on the target atom transforms the CZ gate into a CNOT gate. Combining the CNOT gate with other single-qubit gates like Hadamard and phase gates forms a universal gate set, allowing for the implementation of various quantum algorithms. As a result, many research teams prioritize the implementation of the CZ gate as a fundamental building block in quantum computation.

In addition to the previously mentioned scheme, there have been other works that have successfully implemented high-fidelity CZ gates. In 2019, Mikhail D. Lukin's group demonstrated a protocol utilizing two global laser pulses [4]. Subsequently, Ming-Sheng Zhan's team proposed another method called the single-modulated-pulse off-resonant modulated driving (SORMD) protocol [5]. Both of these approaches allow lasers to interact with atoms simultaneously, eliminating the need to distinguish between control and target atoms, while satisfying the condition mentioned in Eq. 1.3 to achieve the CZ gate.

1.3 Laser Phase and Frequency Noise

The finite phase noise of lasers, which affects the damping of Rabi oscillations, is one factor leading to a decrease in gate fidelity [6]. Although stabilized lasers are used, the limited bandwidth of the feedback loop can result in high-frequency noise that cannot be fully suppressed. To address this issue and achieve good gate fidelity [7], a reference cavity is employed as a spectral filter, effectively suppressing the phase noise induced by frequencies above the lock bandwidth. This approach helps enhance the coherence time, thereby emphasizing the significance of suppressing laser phase noise.

doi:10.6342/NTU202302912

1.3.1 Laser Noise Sources

Diode lasers typically have linewidths in the range of several MHz. To reduce the linewidth, an external cavity can be formed by using a grating, the first diffraction order of the grating is reflected back towards the laser diode. By selecting the wavelength for feedback and achieving resonance between the grating and the rear facet, the optical feedback suppresses the spontaneous emission noise. The external cavity is designed to have a longer length compared to the internal cavity, resulting in a smaller free spectral range (FSR). A grating-stabilized external cavity diode laser (ECDL) with higher finesse has the potential to achieve linewidths narrower than 1 MHz, and it could even reach around 100 kHz. However, despite the improved linewidth, it is still not sufficient for efficient excitation of specific Rydberg states.

For diode lasers, the fundamental linewidth of a free-running laser primarily originates from spontaneous emission, which is a form of quantum noise. This quantum noise is amplified by the gain medium. However, if the losses in the resonant cavity are very low, allowing for high-power operation within the cavity, the impact of quantum noise on the laser is relatively smaller compared to technical noise. In practice, the frequency noise of a laser is predominantly influenced by mechanical fluctuations, which introduce 1/f noise and white noise components. Fig. 1.2 illustrates that in an open-loop configu-

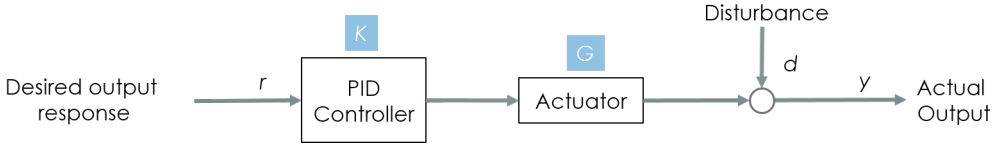

Figure 1.2: In an open-loop system, disturbances couple to the system and affect the output without any feedback control.

ration, the ECDL is sensitive to noise sources arising from external disturbances. In the

doi:10.6342/NTU202302912

case of a laser diode, these disturbances primarily stem from environmental factors, including temperature fluctuations and variations in injection current. Temperature changes directly impact the length and wavelength of the resonance cavity in the diode, while fluctuations in injection current lead to variations in the refractive index of the semiconductor material, thereby modifying the effective cavity length and resulting in output frequency fluctuations. To describe the stability of laser frequency, the laser linewidth is often used.

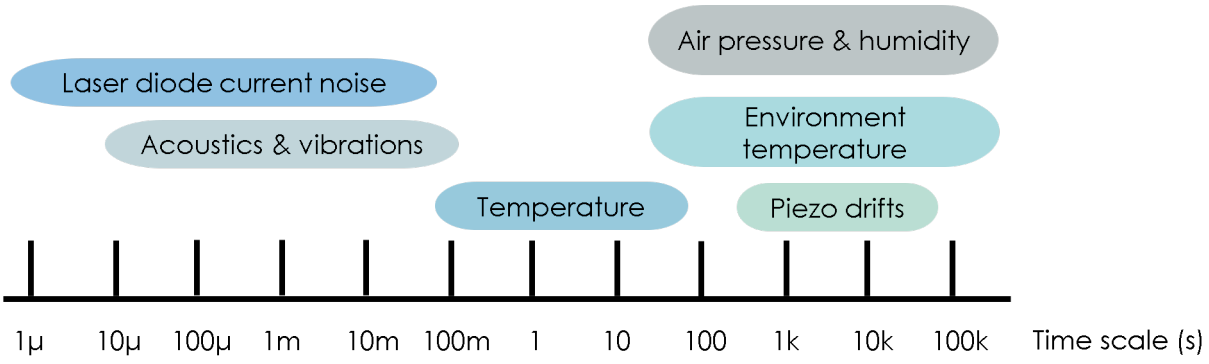

Figure 1.3: Sources of laser noise.

However, the accurate value of the linewidth is not solely determined by the laser itself, but also depends on the measurement time. As shown in Fig. 1.3, different environmental disturbances have varying effects over time. Therefore, if the measurement is conducted on a microsecond timescale, the influence of air pressure fluctuations within that time period may not affect the linewidth of a single measurement. However, it can cause long-term drift or jitter of the central frequency, which can have an impact on measurements conducted over longer durations. Therefore, in addition to frequency domain analysis, time domain analysis is also required to assess laser frequency stability.

doi:10.6342/NTU202302912

1.3.2 Laser Linewidth and Stability

The instantaneous beat frequency obtained from the radio frequency spectrum is [8]

$$\nu(t) = \nu_0 + \frac{1}{2\pi}\frac{d\phi(t)}{dt} = \nu_0 + \Delta\nu(t), \tag{1.4}$$

ν_0 is the beat note signal produced by lasers with a frequency difference, and $\phi(t)$ represents the difference in the individual phases. $\Delta\nu(t)$ is the frequency deviation over the sampling period τ caused by phase noise. In time-domain analysis, the Allan variance is obtained by quantizing measurements or signals and taking consecutive samples at different intervals of τ:

$$\sigma^2(\tau) = \frac{1}{2}\left\langle [\nu_\tau(t) - \nu_\tau(t+\tau)]^2 \right\rangle, \tag{1.5}$$

Where the brackets $\langle\rangle$ denote time averaging.

The power spectral density (PSD) of the frequency noise, measured in Hz^2/Hz, is used to analyze the frequency domain and in terms of Fourier frequency f is given by

$$S_{\Delta\nu}(f) = 2\int_0^\infty \langle \Delta\nu_\tau(t)\Delta\nu_\tau(t+\tau)\rangle\, e^{-i2\pi f\tau} d\tau. \tag{1.6}$$

Consequently, the root mean square (rms) linewidth is

$$\Delta\nu_{rms} = \sqrt{\int_0^\infty S_{\Delta\nu}(f)df}. \tag{1.7}$$

The Allan variance can be calculated by integrating the frequency noise spectrum:

$$\sigma^2(\tau) = 2\int_0^\infty S_{\Delta\nu}(f)\frac{sin^4(\pi f\tau)}{(\pi f\tau)^2}df. \tag{1.8}$$

In general, the frequency noise spectrum cannot be directly obtained from the Allan vari-

doi:10.6342/NTU202302912

ance. Instead, it is preferable to first obtain the frequency noise spectrum.

1.4 Thesis Outline

After discussing the utilization of Rydberg atoms for performing two-qubit gates in quantum information processing and highlighting the importance of laser noise in achieving high gate fidelity, we explore the various sources of noise that can lead to phase noise at different time scales. In Chapter 2, we will introduce closed-loop control systems and their role in laser control. We will also discuss the components and structures involved in the laser control system, with a focus on the Pound-Drever-Hall (PDH) laser frequency stabilization technique. In Chapter 3, we will describe our experimental setup for laser frequency stabilization, including the construction of stable 1039nm and 459nm lasers used to excite atoms to Rydberg states. Both lasers will be locked to the same high-finesse cavity. Subsequently, we will conduct measurements on the cavity and assess the stability of laser locking.

Once the laser locking performance is confirmed, Chapter 4 will focus on using the lasers to excite cesium atoms to Rydberg states. For the 1039nm laser, we will use the transmitted light through the cavity, and we will describe how injection locking is employed as a fiber amplifier seed to achieve higher power. Furthermore, we will utilize Doppler-free saturation spectroscopy to determine the zero-crossing temperature of the cavity and set it at that temperature. Then, we will use this stabilized laser system to excite cold atoms to different Rydberg states. Finally, Chapter 5 will be dedicated to the conclusion of the research.

doi:10.6342/NTU202302912

Chapter 2

Frequency Stabilization of Lasers

Numerous techniques, including atomic spectroscopy, frequency comb, and optical cavity, can be used as frequency references for laser frequency stability. To lock a laser to an atomic spectral line, first excite the atom to a given state, and then use the matching spectral line to lock the laser. However, for two-photon excitation to drive Rydberg states, it is common to choose a detuning at the intermediate state to avoid spontaneous emission. In such cases, relying solely on atomic spectroscopy for laser stabilization may not be the optimal choice. Additional techniques and approaches are often required to achieve stable and precise control of the laser frequency in these scenarios. A stable optical cavity is used as a reference to create a signal for feedback of the laser stability because frequency combs have significantly higher prices than optical cavities. In this chapter, we will discuss the detail of the Pound-Drever-Hall (PDH) locking process that uses an optical resonator for laser stabilization.

doi:10.6342/NTU202302912

2.1 Control System

2.1.1 Closed-Loop System

In an open-loop system, the control actions are determined based on a predefined input, regardless of external disturbances. This lack of feedback makes open-loop systems vulnerable to errors and disturbances. Therefore, in order to compensate for laser phase and frequency noise caused by the environment dynamically, a closed-loop system must be used to provide feedback and control the stability of the laser. The basic closed-loop setup builds upon the open-loop system illustrated in Fig. 1.2. In the closed-loop system, the system output is compared to the desired output, resulting in an error signal. This error signal is then used to adjust the control actions of the controller, completing the closed-loop feedback loop. By continuously monitoring and comparing the actual output with the desired output, the closed-loop system can make real-time adjustments to minimize the error and improve the overall performance and stability of the system.

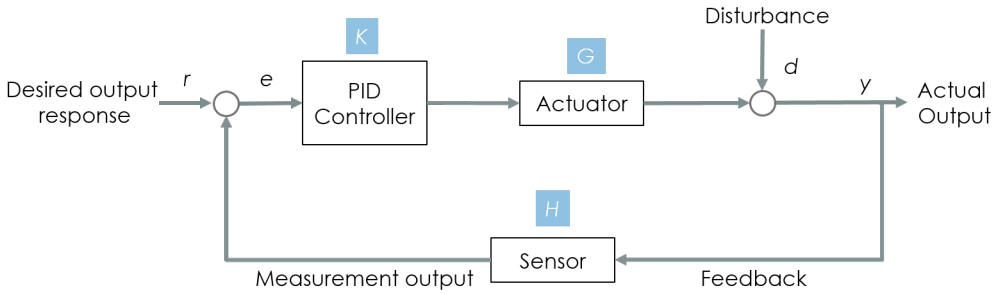

Figure 2.1: In a closed-loop system, the output signal y, which is measured by the sensor H, is compared to the reference input signal r. The difference between the output and the reference input is the error signal e. The error signal is then processed by the controller K to generate control actions. These control actions are sent to the actuator G, which produces the desired output signal y based on the feedback information from the sensor.

According to the setup shown in Fig. 2.1, in a closed-loop system, the output signal y can be measured by a sensor and compared to a reference signal r to generate an error

doi:10.6342/NTU202302912

signal e. This error signal is then input to the controller, which outputs a control signal to the actuator, generating the output signal y. The goal of the entire loop is to make the output signal y match the reference signal r, even in the presence of disturbances or variations. This setup forms a feedback loop, where the sensor, controller, and actuator are adjusted based on system requirements and control objectives. The transfer functions H(s), K(s), and G(s) represent the characteristics and actions of the sensor, controller, and actuator, respectively.

In addition to input signals and feedback information, the consideration of output disturbances is crucial in a system. These disturbances can be noise, environmental changes, or other external factors that impact the system output signal, leading to deviations from the desired response. The relationship between the system output signal and the input signal can be effectively described using transfer functions

$$\begin{aligned} y &= d + G(s)(K(s)e) \\ e &= r - H(s)y. \end{aligned} \tag{2.1}$$

The output disturbance can be expressed as follows:

$$y = \frac{G(s)K(s)}{1 + G(s)K(s)H(s)}r + \frac{1}{1 + G(s)K(s)H(s)}d = T(s)r + S(s)d. \tag{2.2}$$

In the given equation, the transfer functions before d and r can be referred to as the disturbance transfer function $S(s)$ and the reference transfer function $T(s)$, respectively. The transfer function $S(s)$ characterizes the sensitivity of the control system to disturbances affecting the output. It reveals how the system reacts to changes in the environment. When the controller gain is sufficiently large and the transfer function H(s) is equal to 1, the output signal closely tracks the reference signal, effectively suppressing any disturbances.

doi:10.6342/NTU202302912

2.1.2 Loop Stability

According to Eq. 2.2, the denominator of the closed-loop transfer function is the same, and the closed-loop poles occur at the positions where the denominator is equal to 0. Therefore, we can find the closed-loop poles by solving the characteristic equation

$$1 + G(s)K(s)H(s) = 0. \tag{2.3}$$

By defining the loop transfer function as $L(s) = G(s)K(s)H(s)$, a feedback control system is stable if all the poles of $L(s)$ are negative real values. Ensuring that the phase condition Arg$[L(s)]$ of the loop transfer function $L(s)$ is less than 180° is a crucial criterion for stability. If the overall phase delay exceeds 180°, the magnitude of the denominator $1 + L(s)$ can become very small, leading to a positive feedback loop gain that amplifies deviations from the reference value. This situation can lead to instability in the feedback system, resulting in the appearance of a ”servo bump” in the spectrum. In this region, the phase approaches 180°, leading to an increase in noise instead of being suppressed. If the loop gain is increased, the system will oscillate in this region, exhibiting high peaks, and the oscillation frequency approximately indicates the bandwidth of the servo system.

2.2 Laser locking system

For a basic laser locking system, it is necessary to generate an error signal and send it to the servo to control the actuator and stabilize the laser frequency output.

doi:10.6342/NTU202302912

2.2.1 Frequency Discriminator

In frequency stabilization methods, atomic or molecular transition frequencies or the resonant frequency of a cavity are often used as frequency discriminators to provide an ” error signal.” The frequency discriminator can be seen as an optical frequency-to-voltage converter, and its output signal has a monotonic slope. This means that when the laser frequency changes, the output of the ”error signal” will also change with a clear slope. This characteristic allows us to accurately read the frequency variations and make precise frequency stabilization adjustments.The thesis utilizes a high-finesse cavity with the Pound-Drever-Hall technique to generate a frequency discriminator.

2.2.2 Actuator

The output signal from the discriminator is then sent to one or multiple laser actuators, which can be finely controlled using voltage signals. These actuators encompass adjustments to the diode temperature and current, along with piezoelectric transducers (PZT). However, due to different response speeds of the actuators, each actuator has its own operating bandwidth. For example, adjusting the temperature of the diode usually requires a longer time to reach equilibrium, and therefore, it is not instantaneously controlled in the feedback system.

PZT is a piezoelectric component that is typically mounted on the grating. It can tune the frequency of the output light by adjusting the position and angle of the grating in response to variations in the piezoelectric voltage. Because PZT is a mechanical part with a feedback bandwidth that is typically in the kHz range, it is suitable for compensating slower frequency drifts. On the other hand, adjusting the current of the laser diode allows

doi:10.6342/NTU202302912

for rapid changes in its output frequency, providing a feedback bandwidth of several MHz. This feature makes it well-suited for delivering high-speed feedback, effectively reducing the laser linewidth.

By combining these two feedback methods, a broadband feedback control system is achieved, enhancing both the frequency stability and linewidth of the laser. The combination of these two feedback methods overcomes the slow response of PZT while maintaining high-speed feedback capability, enabling effective compensation for frequency variations at different time scales.

2.2.3 PID Servo

The PID controller is a commonly used controller that consists of three components: proportional (P), integral (I), and derivative (D). The output signal of the PID controller is a combination of these three components, resulting in a controlled output signal

$$K_P e(t) + K_I \int_0^t d\tau e(\tau) + K_D \frac{de(t)}{dt}. \tag{2.4}$$

After performing the Laplace transform, the transfer function of the PID controller is given by

$$K(s) = K_P + \frac{K_I}{s} + K_D s. \tag{2.5}$$

The integral part K_I accumulates the error to generate a control signal, reducing the steady-state error of the system. It introduces a phase delay of 90° between the output and input, primarily controlling low-frequency signal gain, which helps eliminate steady-state errors. On the other hand, the derivative part K_D generates a control signal based on the rate of change of the error signal, enabling it to anticipate future trends in the system. Its

doi:10.6342/NTU202302912

gain primarily affects high-frequency signals and can be used to increase damping and sensitivity to noise. The output phase will lead the input by 90°. By adjusting the values of K_P, K_I, and K_D, the PID controller is tuned to achieve the desired system control output.

2.3 High Finesse Cavity

In order to work effectively for feedback loops, a stable reference provides us with a baseline to compare with the system output. An approach that can be used to achieve our experimental requirement is to utilize the resonances of a Fabry-Pérot cavity. This type of cavity consists of two parallel mirrors that are separated by a distance. The cavity produces discrete resonances at discrete frequencies as light enters and escapes through the mirrors. By locking the feedback loop to these specific frequencies, a highly stable reference can be established, allowing for the feedback loop to function more effectively and accurately.

2.3.1 Light Propagation in Optical Cavity

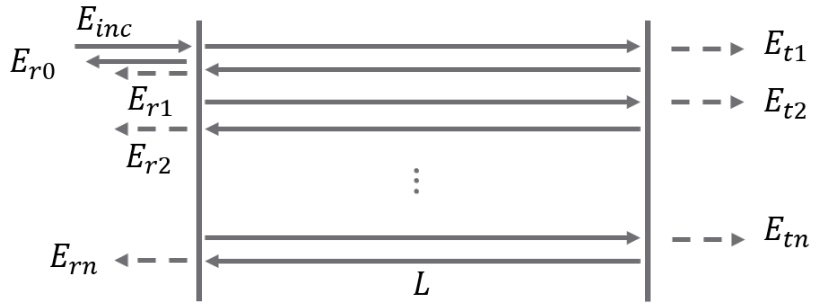

Figure 2.2: The propagation of an incident beam as it travels through a Fabry-Pérot resonator.

When a laser beam is perfectly matched and incident on two mirrors, it undergoes

doi:10.6342/NTU202302912

constructive interference within the optical cavity, amplifying the power of the laser. Consequently, only specific frequencies can resonate and propagate when the distance between the mirrors is an integer multiple of half the laser wavelength. This condition ensures that the laser light constructively interferes within the optical cavity.

When an electric wave with an amplitude of E_0 and an angular frequency of ω propagates in a cavity with a distance of L between two mirrors, the light acquires a single-pass phase shift ϕ at a frequency of ν between the mirrors.

Since $2L$ is the round-trip path length, the round-trip time for light traveling through the resonator is expressed as $T_{RT} = \frac{2L}{c}$. The free spectral range (FSR) of an optical system is the distance between frequency peaks and is denoted by the inversion of T_{RT}. The accumulation of phase shifts that occur during a round trip at a certain frequency is referred to as

$$2\phi(\nu) = 2\pi\nu T_{RT} = 2\pi\nu\frac{1}{\nu_{FSR}}. \tag{2.6}$$

The electric field of the incident light can be written as

$$E_{inc} = E_0 e^{i\omega t}. \tag{2.7}$$

Let t_1 and t_2 represent the electric field transmissions of two mirrors, and r_1 and r_2 denote their respective electric field reflectivities. Consider the additional phase shift of $e^{i\frac{\pi}{2}} = i$ that occurs each time a signal passes through a mirror [9][10]. On the other hand, the electric field reflects off from the side with the lower index of refraction, and the reflected wave similarly causes a phase change for $e^{i\pi} = -1$. The direct electric field reflected from the first mirror is

$$E_{r0} = -r_1 E_{inc}. \tag{2.8}$$

doi:10.6342/NTU202302912

The electric field that goes through the first mirror and is reflected by the second mirror is represented as

$$E_{r1} = t_1^2 r_2 e^{i2\phi} E_{inc} \tag{2.9}$$

and

$$E_{r2} = t_1^2 r_2^2 r_1 e^{i2(2\phi)} E_{inc}. \tag{2.10}$$

Following several reflections inside the cavity, more light is reflected, and from this we obtain contributions

$$E_{rn} = t_1^2 r_2^n r_1^{(n-1)} e^{i2n\phi} E_{inc}. \tag{2.11}$$

Add all of the reflected light contributions to

$$\begin{aligned} E_{refl} &= E_{inc}[-r_1 + t_1^2 r_2 e^{i2\phi}(1 + r_1 r_2 e^{i2\phi} + ... + (r_1 r_2)^{n'} e^{i2n'\phi})] \\ &= E_{inc}(-r_1 + \frac{r_2 t_1^2 e^{i2\phi}}{1 - r_1 r_2 e^{i2\phi}}). \end{aligned} \tag{2.12}$$

The total reflection beam needs to consider the reflection coefficient $F(\omega)$

$$F(\omega) = E_{refl}/E_{inc} = \frac{-r_1 + r_2(r_1^2 + t_1^2)e^{i2\phi}}{1 - r_1 r_2 e^{i2\phi}}. \tag{2.13}$$

Assuming the simplest case for a lossless cavity with $r_1 = r_2 = r$ and $t_1 = t_2 = t$. Replace the phase shift using Eq. 2.6 and for a lossless mirror $r^2 + t^2 = R + T = 1$, we can get the reflection coefficient

$$F(\omega) = E_{refl}/E_{inc} = \frac{r(e^{i\frac{\omega}{\nu_{FSR}}} - 1)}{1 - r^2 e^{i\frac{\omega}{\nu_{FSR}}}} \tag{2.14}$$

doi:10.6342/NTU202302912

2.4 Pound-Drever-Hall (PDH) Locking Technique

The Pound-Drever-Hall method is based on a simple concept that involves measuring the frequency of a laser using a Fabry-Perot cavity and then utilizing this measurement to provide feedback to reduce frequency fluctuations. This technique employs a type of null lock-in detection to collect and analyze a specific signal of interest while limiting the influence of noise or other undesired signals. The simplest scheme is illustrated in Fig. 2.3 [11].

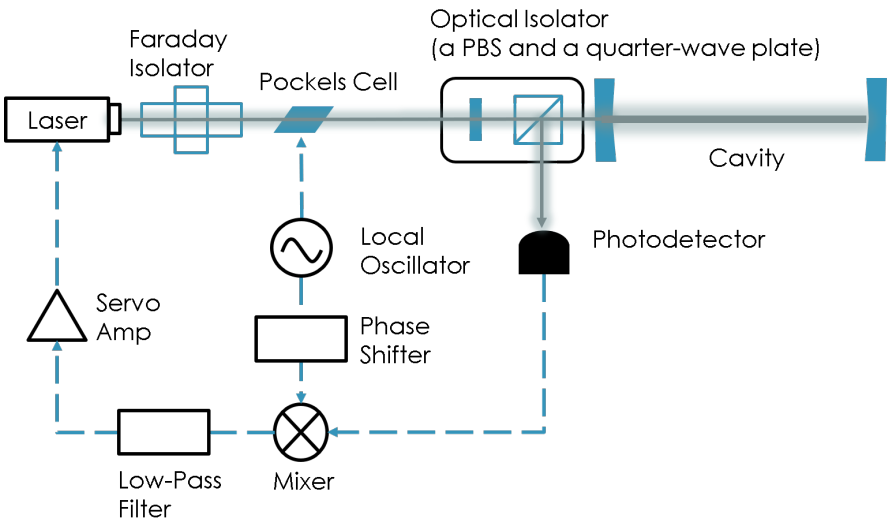

Figure 2.3: The fundamental design for locking a cavity to a laser. Optical paths and Signal pathways are denoted by solid and dotted lines, respectively.

2.4.1 Phase Modulation

The Pound-Drever-Hall method allows us to detect the phase of the reflected beam, which is necessary for determining whether the laser frequency is higher or lower than the cavity resonance. The total reflected power displays a beat pattern at the modulation frequency, and sidebands with a definite phase relationship are produced when the laser frequency is modulated. The laser diode injection current exhibits amplitude modulation

doi:10.6342/NTU202302912

in addition to phase modulation. As a result, an extra fiber-EOM is employed in experiments to modulate the phase. Therefore, the phase-modulated electric field output after the beam has traveled through the Pockels cell is

$$E = E_0 e^{i(\omega t + \beta sin(\Omega t))}, \tag{2.15}$$

where ω is the angular frequency of the carrier and Ω is the modulation frequency; as a result, the two first-order sidebands are at $\omega \pm \Omega$. β is the modulation depth of fiber-EOM, which we can control by adjusting the RF output power, and $J_k(\beta)$ is the Bessel function of order k. For Fourier decomposition

$$e^{i\beta sin\omega t} = \sum_{n=-\infty}^{\infty} J_n(\beta) e^{i\omega t} \sim J_0(\beta) + J_1(\beta) 2isin\omega t. \tag{2.16}$$

To describe using the Bessel function as

$$E = E_0 e^{i\omega t} \left\{ J_0(\beta) + \sum_{k=1}^{\infty} J_k(\beta) e^{ik\Omega t} + \sum_{k=1}^{\infty} (-1)^k J_k(\beta) e^{-ik\Omega t} \right\}. \tag{2.17}$$

In the case where $\beta < 1$, power is concentrated on the carrier and first-order sidebands,

$$P_c + 2P_s = J_0^2(\beta) + 2J_1^2(\beta) \approx P_0. \tag{2.18}$$

The reflected electric field is calculated by multiplying each beam separately by its reflection coefficient at the appropriate frequency.

$$\begin{aligned} E_{refl} = E_0 [& F(\omega) J_0(\beta) e^{i\omega t} + F(\omega + \Omega) J_1(\beta) e^{i(\omega + \Omega)t} \\ & + F(\omega - \Omega) J_1(\beta) e^{i(\omega - \Omega)t}], \end{aligned} \tag{2.19}$$

doi:10.6342/NTU202302912

where $F(\omega)$ represents the reflection coefficient in Eq. 2.14. The measured reflected power by a photodetector is

$$\begin{aligned} P_{refl} &= |E_{refl}|^2 \\ &= P_c|F(\omega)|^2 + P_s\{|F(\omega+\Omega)|^2 + |F(\omega-\Omega)|^2\} \\ &+2\sqrt{P_cP_s}\{Re[F(\omega)F^*(\omega+\Omega) - F^*(\omega)F(\omega-\Omega)]cos(\Omega t) \\ &+Im[F(\omega)F^*(\omega+\Omega) - F^*(\omega)F(\omega-\Omega)]sin(\Omega t)\} + (2\Omega terms). \end{aligned} \tag{2.20}$$

The presence of the 2Ω terms arises from the interference between the sidebands themselves. In the analysis, we are only concerned with the interference between the carrier and the sidebands of the signal, which is described by the Ω terms.

2.4.2 Demodulation

Simplifies the following discussion by replacing $F(\omega)F^*(\omega+\Omega) - F^*(\omega)F(\omega-\Omega)$ with $\chi(\omega)$. The expression within the brackets can then be replaced with $Re[\chi(\omega)]cos(\Omega t) + Im[\chi(\omega)]sin(\Omega t)$. These terms contain sine and cosine components, which allow us to demodulate the photodiode signal by mixing it with a reference frequency Ω':

$$\begin{aligned} &Re[\chi(\omega)]cos(\Omega t)sin(\Omega' t+\phi) + Im[\chi(\omega)]sin(\Omega t)sin(\Omega' t+\phi) \\ &= \frac{1}{2}Re[\chi(\omega)]\{sin[(\Omega+\Omega')t+\phi] - sin[(\Omega-\Omega')t-\phi]\} \\ &+\frac{1}{2}Im[\chi(\omega)]\{cos[(\Omega-\Omega')t-\phi] - cos[(\Omega+\Omega')t+\phi]\}. \end{aligned} \tag{2.21}$$

Assuming the carrier is near resonance and the modulation frequency is large enough to completely reflect the sidebands ($F(\omega \pm \Omega) \approx 1$). For modulation frequencies Ω higher than the cavity linewidth $\delta\nu_c$, only a purely imaginary part is left [11].

When $\Omega = \Omega'$, a low-pass filter can be used to remove the sum frequency term, leav-

doi:10.6342/NTU202302912

ing only the DC term. The phase shifter allows for the transformation of sine and cosine components due to different delays in the two signal paths. If the modulation frequency is high enough ($\Omega \gg \delta\nu_c$) and the carrier is close to resonance ($F(\omega \pm \Omega) \approx 1$), the sidebands are almost totally reflected. As a result, for high modulation frequencies, only a purely imaginary component remains as $\chi(\omega) \approx -i2Im[F(\omega)]$. The error signal is

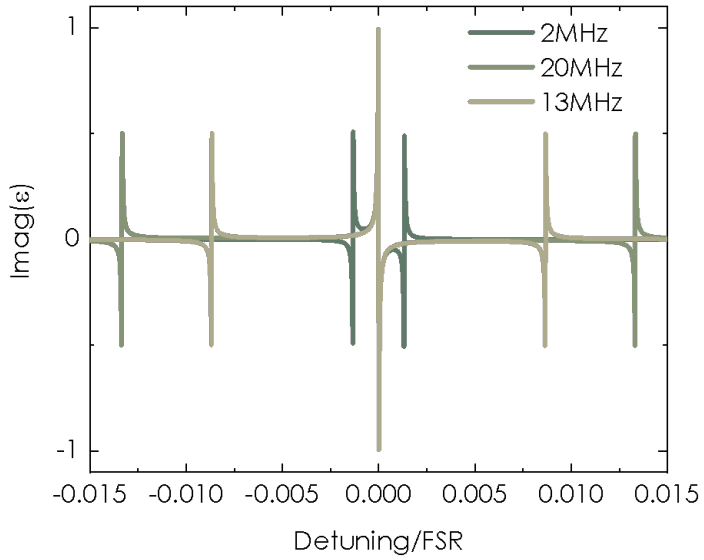

Figure 2.4: The simulation involves varying the modulation frequency to observe changes in the imaginary part of the error signal.

$$\epsilon = -2\sqrt{P_c P_s} Im\{F(\omega)F^*(\omega+\Omega) - F^*(\omega)F(\omega-\Omega)\}. \tag{2.22}$$

Fig. 2.4 shows the plot of the imaginary part of the error signal, calculated using Eq. 2.22, with varying modulation frequencies generated by the Pockels cell. If the deviation from resonance of the laser frequency in a high-finesse cavity is small enough in comparison to the cavity linewidth, the error signal will approximate linear behavior at the resonance peak.

$$\epsilon = D\delta f \tag{2.23}$$

doi:10.6342/NTU202302912

A definition for the proportionality constant is "frequency discriminant"

$$D = -\frac{8\sqrt{P_c P_s}}{\delta\nu_c} = -\frac{16\mathcal{F}LP_0}{c} J_0(\beta)J_1(\beta). \tag{2.24}$$

By combining Eq. 2.6 with the finesse $\mathcal{F} = \nu_{FSR}/\delta\nu_c$, we can deduce that the frequency discriminant, representing the slope of the error signal, is affected by two key factors: the cavity linewidth and the modulation depth of the EOM. As depicted in Fig. 2.5 (a), the slope of the error signal is visually affected by the cavity linewidth. A narrower linewidth leads to a steeper slope, particularly near the resonance of the cavity. Furthermore, Fig. 2.5 (b) demonstrates that the modulation depth β determines the power distribution between the carrier and sidebands. It reveals that there exists an optimal modulation depth that maximizes the slope of the error signal.

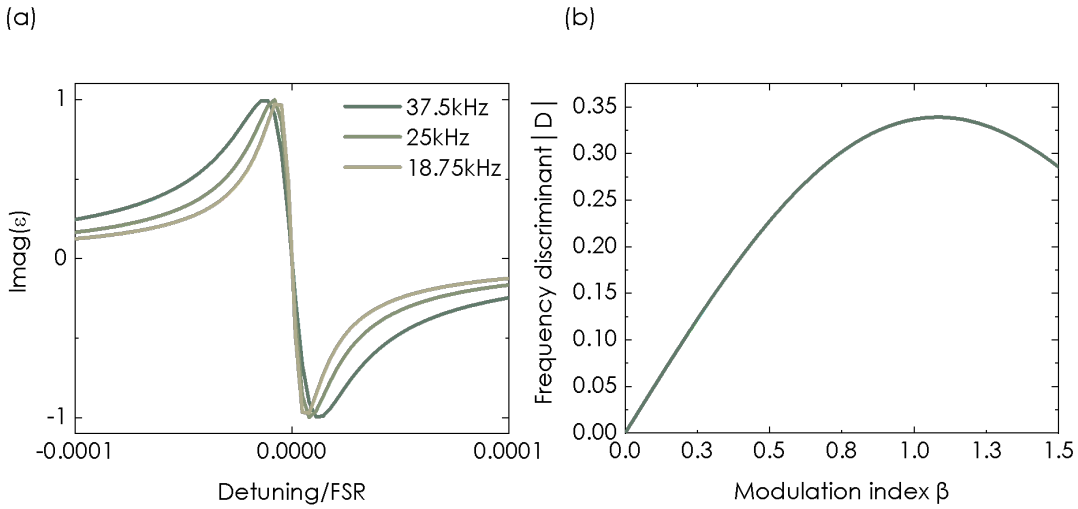

Figure 2.5: (a) The imaginary part of the error signal with a narrower cavity linewidth has a higher magnitude for the frequency discriminant. (b) The modulation index also affects the frequency discriminant, with the maximum occurring at $\beta = 1.08$.

2.4.3 Frequency Offset Locking Technique

Due to the fact that the resonance frequency of the cavity may not necessarily match the required frequency for Rydberg excitation, we can employ the frequency offset locking

doi:10.6342/NTU202302912

technique by using dual frequency modulation to lock the 918nm laser.

The electric field of the incident light can be written as

$$E_{inc} = E_0 e^{(i\omega_0 t + i\beta_1 sin\omega_1 t + i\beta_2 sin\omega_2 t)} \tag{2.25}$$

The phase modulation yields a carrier at angular frequency ω_0, sidebands at angular frequencies $\omega_0 + \omega_1$ and $\omega_0 - \omega_1$, and sub-sidebands at $\omega_0 + \omega_1 \pm \omega_2$ and $\omega_0 - \omega_1 \pm \omega_2$. This technique involves phase modulation using two sinusoidal signals with depths β_1 and β_2 and angular frequencies ω_1 and ω_2, respectively. The modulation scheme aims to generate sidebands at frequencies $\omega_0 \pm \omega_1$ and one of the sidebands is selected to match the resonant frequencies of the cavity. By utilizing ω_2 for demodulation of the reflected power, an error signal is generated. The frequency discriminant can be expressed as follows [12]:

$$D_{DSB} = \frac{16\mathcal{F}LP_0}{c} J_1^2(\beta_1) J_0(\beta_2) J_1(\beta_2). \tag{2.26}$$

doi:10.6342/NTU202302912

doi:10.6342/NTU202302912

Chapter 3

Experimental Realisations

In this chapter, we present the setup of the entire Rydberg laser system. To minimize vibrations from the optical table, we place both Rydberg lasers and the ultra-low expansion (ULE) cavity on the same optical breadboard (Newport M-PG-34-4-ML). We will provide a detailed description of the laser locking procedure, assess the locking performance, and discuss the cavity measurement.

3.1 ULE Cavity in the Vacuum System

We utilize a Fabry-Pérot (F-P) cavity manufactured by Stable Laser Systems. The cavity is constructed using ultra-low expansion (ULE) glass, which allows its heat expansion coefficient to approach zero when operated at the zero crossing temperature of the cavity. Because the temperature-controlled F-P cavity is intended to avoid circumstantial fluctuation, it is housed in a chamber. As the roughing pump, we utilize a dry scroll vacuum pump (Qualytest HLT260), and then put on an external turbo pump to reduce the pressure to roughly 10^{-6} torr. Following that, in the baking process, we must carefully

doi:10.6342/NTU202302912

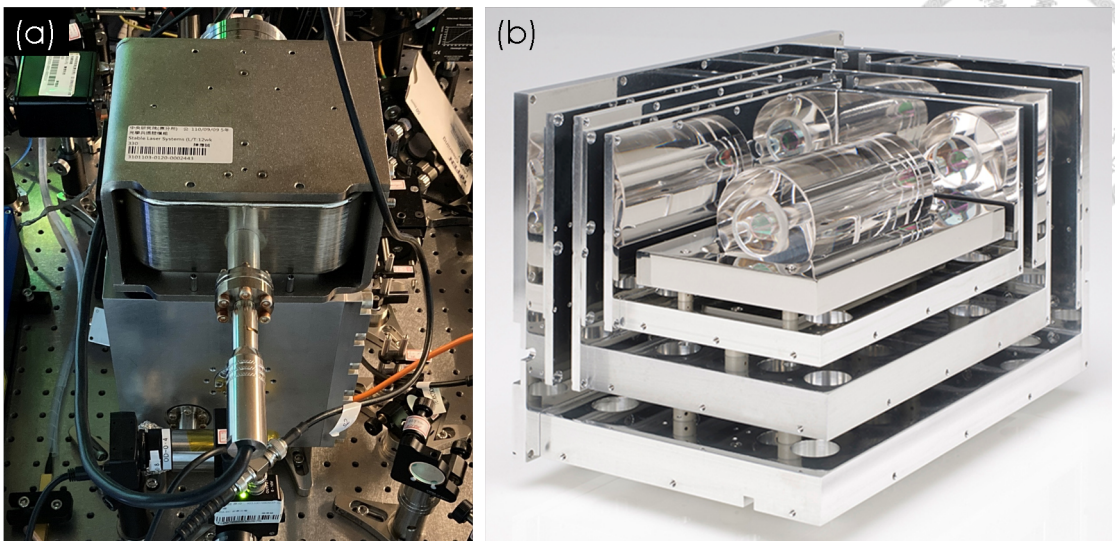

Figure 3.1: (a) Our temperature-controlled vacuum cavity system incorporates notched cavity and multistage cavity housings. (b) The internal structure of the multistage cavity housings is shown in the image from the website of Stable Laser Systems.

heat the chamber to avoid a significant increase in water gas to fast boost air pressure. Finally, activate the ion pump and halt baking when the pressure stabilizes. The F-P cavity is housed in a low-pressure chamber with a pressure of 10^{-7} torr.

3.1.1 Mode Matching

To achieve mode matching, the spatial and phase characteristics of the laser beam must match the resonant cavity; in other words, the geometry of the cavity and the beam must be taken into account while mode matching. This alignment maximizes the power of the spatial mode that we want to use in the subsequent experiment by efficiently coupling the laser beam into the cavity.

The ray transfer matrix approach can be used to analyze beam-transmission qualities, and the complex beam parameter, q-parameter, contains information about Gaussian beams, with the size and curvature of the beam given by this complex-valued parameter.

doi:10.6342/NTU202302912

$$\frac{1}{q(z)} = \frac{1}{R(z)} + i\frac{\lambda}{\pi w^2(z)}, \tag{3.1}$$

where λ is the wavelength of the Gaussian beam, w is the beam radius, and R is the radius of curvature (ROC) of the wavefronts. Both can be written as

$$R = \frac{1}{Re(q^{-1})} \tag{3.2}$$

and

$$w = \sqrt{\frac{\lambda}{\pi Im(q^{-1})}}. \tag{3.3}$$

The following equation describes how light moves through an optical component or an optical system that is expressed in terms of ABCD matrices.

$$q' = \frac{Aq + B}{Cq + D} \tag{3.4}$$

The F-P cavity is 100mm long, and the mirror pair will consist of a plane mirror on one side and a 50cm ROC (radius of curvature) mirror on the other. To accommodate the curved mirror, we must change the beam size of the input light to correspond to the spatial mode of the cavity TEM_{00}. Because the curvature of a pair of mirrors affects the evolution of the beam radius and ROC, we can modify the input beam size to change the wavefront curvature to fit the ROC mirror.

To conduct mode matching, several alternative lens systems can produce the same ABCD matrix; in this case, I simply utilize a lens to focus the beam.

When we consider a laser beam that has a plane wavefront and it is incident on a thin lens, and we are given the laser beam size w_1 and the lens focal length f, then under the

doi:10.6342/NTU202302912

condition $z_{R_1} \gg f$, we may obtain the beam size w_2 at the focal plane after it has passed through the lens [13]:

$$w_2 = \frac{\lambda f}{\pi w_1 [1 + (\frac{f}{z_{R_1}})^2]^{1/2}} \approx \frac{\lambda f}{\pi w_1}. \tag{3.5}$$

We can use a CCD in the experiment to measure the size of the light spot before the lens. If the angle of divergence is small enough and the Rayleigh length is very long, the incident light in front of the lens can be regarded as a simple plane wave. As a result, the estimated value of Eq. 3.5 allows us to estimate the focus of the lens we can utilize for cavity mode matching.

During the mode matching procedure, intensity patterns of several spatial modes are observed in Fig. 3.2.

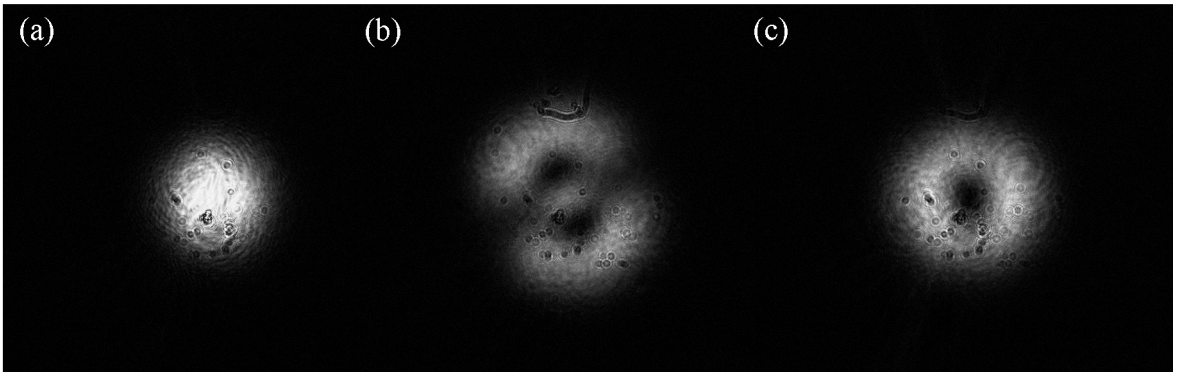

Figure 3.2: Patterns of intensity for a few various spatial modes during the mode matching procedure.

3.2 Rydberg Laser Experimental Setup

It takes an ultraviolet wavelength to transition from the ground state to the Rydberg state, but fiber losses pose a significant technical challenge. As a solution, a two-photon

doi:10.6342/NTU202302912

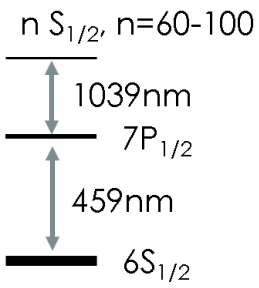

Figure 3.3: Two-photon excitation configuration for driving cesium atoms to Rydberg states. The 459nm laser is used to drive the transition from $6S_{1/2}$ to $7P_{1/2}$, while the 1039nm laser is used for the transition from $7P_{1/2}$ to the Rydberg state.

transition is utilized to reach the Rydberg state via an intermediate state. We used a 459nm laser to drive the $6S_{1/2}$ to $7P_{1/2}$ transition, then a 1039nm laser for the $7P_{1/2}$ to $nS_{1/2}$ $(n = 60 - 100)$ transition. The $7P_{1/2}$ state is chosen as the intermediate state to minimize scattering, as its lifetime is longer than that of the $7P_{3/2}$ state. Additionally, a higher optical power laser can be obtained easier from the intermediate state to drive the Rydberg transition.

3.2.1 1039nm Rydberg Laser

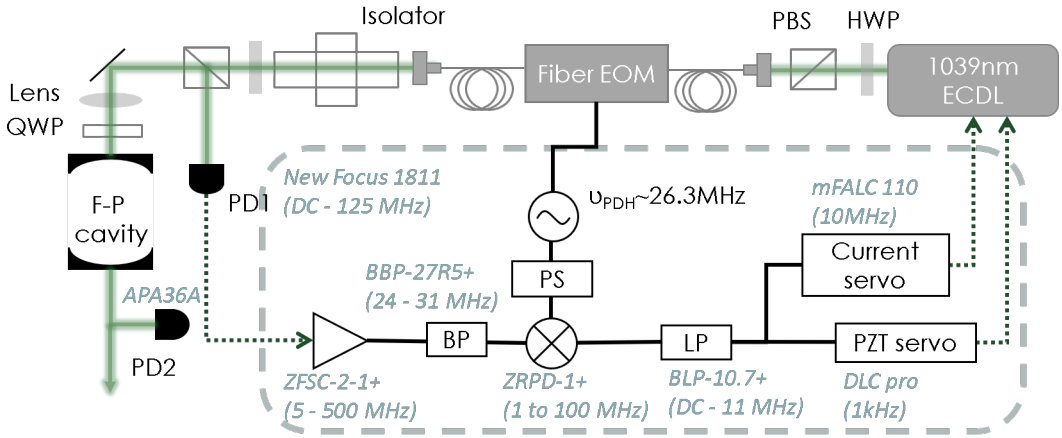

Figure 3.4: 1039nm laser system experimental setup for the PDH lock. ECDL, external cavity diode laser; F-P cavity, Fabry – Pérot cavity; PZT, piezo actuator; HWP, half-wave plate; QWP, quarter-wave plate; PBS, polarizing beam splitter; Fiber-EOM, Fiber-Coupled electro-optic modulator; BP, bandpass filter; LP, low-pass filter; PS, phase shifter; PD, photodiode

The complete setup for the 1039nm laser is depicted in Fig.3.4. In the initial stage,

doi:10.6342/NTU202302912

the ECDL (Toptica DL pro) with a maximum output power of greater than 100mW is used, with an input power of 15mW coupled into a fiber-coupled EOM. A pair of cylindrical lenses is employed to shape the output beam from the ECDL. A half-wave plate and a PBS are utilized to split off some power for wavelength monitoring. An HWP is placed before the EOM to adjust the polarization and match it to the PM fiber, as the crystal inside the EOM requires a specific polarization input.

The phase modulation is achieved using a fiber-coupled EOM (EOSPACE PM-0S5-10-PFA-PFA-106-UL), where the refractive index of the light changes by applying an RF voltage. This causes variations in the optical path length and results in an initial phase shift. As the voltage is increased, the delayed phase shift becomes proportional to the voltage, thus leading to changes in the instantaneous frequency, which is defined as the time derivative of the phase. Applying sinusoidal phase modulation results in sinusoidal frequency modulation at a frequency $\Omega = 26.3\text{MHz}$.

Compared to a free-space EOM, the fiber-coupled EOM requires a much lower modulation RF voltage to achieve the same optical phase shift. It is also possible to simultaneously couple two modulation frequencies to avoid the need for multiple free-space EOMs. This advantage can be utilized for frequency offset locking (Sec. 2.4.3) and FSR locking (Sec. 3.5.2).

The laser beam output from the fiber-EOM closely resembles the TEM_{00} mode, and an isolator is employed to prevent any reflected light from entering the F-P cavity. The half-wave plate and PBS are used to adjust the power input to the cavity to a level below 1mW. This is important because excessive power resonating in a high-finesse cavity can cause thermal shifts in the cavity resonance[14][15][16]. The lens placed after this stage

doi:10.6342/NTU202302912

is used for mode matching with the F-P cavity, and the choice of its focal length is determined and calculated as described in Sec. 3.1.1. By passing through a QWP, the light's polarization is transformed from horizontal to 45°, and when the light reflected from the F-P cavity is recombined with the original beam, it passes through the QWP once more, resulting in vertical polarization. This allows the reflected light from the cavity to be directed into a high-bandwidth photodiode (New Focus 1811) by the PBS.

The reflected signal is received and then passed through electronic components, including filters and mixers, for demodulation to obtain a high S/N error signal. This error signal is then fed into the current (Toptica mFALC 110) and PZT servo (DLC pro) to control the signal. The components used in this setup are shown in Fig. 3.4, and we will provide a detailed discussion in Sec. 3.3.

3.2.2 459nm Rydberg Laser

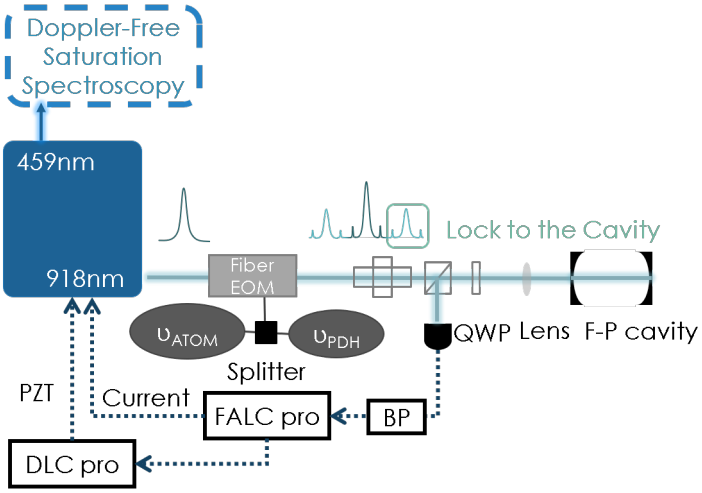

Figure 3.5: The setup for the 918nm laser uses offset locking to stabilize the frequency.

A Toptica DLC-TA-SHG pro-SHG laser to generate 459nm light for the Rydberg laser. The main elements of the laser system are a grating-stabilized diode laser (Master Oscillator), a tapered amplifier (TA), and a second harmonic generation (SHG) cavity.

doi:10.6342/NTU202302912

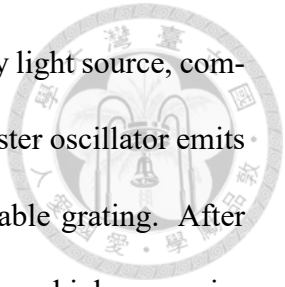

An ECDL, configured in a Littrow configuration, serves as the primary light source, commonly referred to as the master oscillator, in the laser system. The master oscillator emits light at a wavelength of 918 nm, which can be adjusted using a tunable grating. After the light from the master oscillator is injected into the TA, it produces a high-power infrared light with a maximum output of approximately 3 W. The infrared beam then passes through a nonlinear crystal within the SHG cavity, resulting in the generation of frequency-doubled laser light at 459 nm. When locked to the PDH error signal that is produced within the commercial laser system, the power of this blue light can reach roughly 1.5 W.

The 918nm laser is also locked to the same F-P cavity for stabilization purposes. However, to ensure that the frequency of the 459nm laser is close to the $6S_{1/2}$ to $7P_{1/2}$ transition, we use the offset locking technique discussed in Sec. 2.4.3. Based on our estimation, the required frequency of the master laser deviates from the cavity resonance by approximately 200MHz. To achieve this frequency offset, we utilize a power splitter (ZFSC-2-1+) to combine the offset frequency with the 25MHz modulation frequency, and then apply this combined signal for modulation to the fiber-EOM (EOSPACE PM-0S5-10-PFA-PFA-910-UL). The reason for choosing a power splitter instead of an RF coupler is due to the high power attenuation of one of the input frequencies by the RF coupler. The reflected signal is detected using a New Focus 1801 detector, and then it passes through a bandpass filter (ZABP-16+) to obtain a low noise signal. This signal is sent into the controller (Toptica FALC pro), which includes a mixer for demodulation and generates a control signal. K_I and K_D are adjusted by the controller to control the current loop and PZT loop (DLC pro).

doi:10.6342/NTU202302912

3.3 RF Layout

The layout of RF circuit components for the 1039nm laser is shown in Fig. 3.10. The complete layout includes the RF circuit elements for demodulation and measuring the cavity FSR, as described in Sec. 3.5.2. Unlike the simplest setup, in experiments aiming to generate high signal-to-noise ratio signals, it is often necessary to amplify or filter the original signal from the detector in order to minimize electronic noise introduced by the RF circuit components.

3.3.1 RF Oscillator

PDH laser locking typically involves the use of higher modulation frequencies, typically in the range of several megahertz. High modulation frequencies reduce low-frequency noise and disturbances, improving signal-to-noise ratio. Because the signal is modulated at a higher frequency, it helps isolate the desired information from noise components at lower frequencies. The feedback loop also responds faster with higher modulation frequencies. The modulation frequency determines how rapidly the control system can track and modify the laser frequency, improving stability and correction speed.

In our experimental setup, we utilize three different signal generators for various purposes. For the 1039nm laser system, the RIGOL DG4162 (160MHz function generator) is employed for PDH error signal generation. The Agilent E4435B (2.0GHz RF signal generator) is used for FSR error signal generation, and it offers superior performance compared to the VCO (CVCO55CC-1443-1523). On the other hand, for the 918nm laser, both the local oscillator signal and the modulation signal for the fiber-EOM are obtained from the

doi:10.6342/NTU202302912

Toptica PDH module embedded in the DLC pro.

To ensure frequency stability and minimize frequency instability between the two signals, an additional rubidium (Rb) atomic clock (FS725) is utilized. All signal generators in the setup are connected to this atomic clock. The output frequency of the atomic clock serves as a stable reference signal for the frequency output of the signal generators. By synchronizing the signal generators to this stable reference signal, the system maintains a high degree of frequency stability, reducing any frequency differences between the two signals and ensuring accurate and reliable operation.

3.3.2 Phase Shifter

The Phase shifter is utilized to compensate for the path mismatch between the received signal from the detector and the demodulated signal, which leads to the error signal mentioned in Eq. 2.21. The magnitude of the error signal at the resonance is desired to be maximized, as it corresponds to the maximum slope. However, in practical experiments, the error signal can be affected by laser phase noise, making it difficult to visually determine the point of maximum slope. However, we have modified the method of adjusting the phase shifter. Instead, we now aim to minimize the error signal at the resonance point. By doing so, the cosine function within the phase-shifted signal compensates for the phase, effectively transforming into a sine function. By subsequently adding or subtracting a 90° phase shift, the signal is restored to its maximum value. At this point, the error signal is ready to be prepared and fed into the servo system as the input signal.

To adjust the phase, when there is only one channel output from the signal source in the experimental setup, it can be split using a power splitter. In the local oscillator

doi:10.6342/NTU202302912

path, a phase shifter with the corresponding frequency is added. For FSR locking, we use the Mini-Circuits SPHSA-152+ phase shifter. The phase adjustment is achieved by controlling an additional DC voltage to control the corresponding phase shift.

In PDH error signal generation, we utilize a function generator with two output channels as an RF oscillator in the setup. One channel generates the modulation frequency for the fiber-EOM, while the other channel serves as the local oscillator for demodulation. During the demodulation process, any original phase difference between the two signals caused by the path can be adjusted by manipulating the phase. By accurately adjusting the phase, we can mitigate these fluctuations and reduce the impact of noise on the error signal. This leads to a higher signal-to-noise ratio, enhancing the overall performance of the system.

3.3.3 Mixer

When choosing a mixer for various applications, it is important to consider several factors. The selection depends on the specific requirements of the application. Three key considerations are bandwidth, LO level, and LO isolation.

The bandwidth of the mixer is crucial and depends on the intended use. For demodulation purposes, the intermediate frequency (IF) output bandwidth of the mixer should encompass the DC signal, which is mentioned in Sec. 2.4.2. Alternatively, a phase detector can be utilized as a multiplier to extract the DC signal. On the other hand, if the mixer is employed to generate the difference or sum frequency of two input signals, the output bandwidth only needs to cover the desired output frequency.

The LO level is another important factor to consider. It determines the driving power

doi:10.6342/NTU202302912

of the local oscillator and affects the conversion efficiency of the mixer. Therefore, the LO level should be chosen appropriately to optimize the performance of the mixer.

Lastly, selecting a mixer with good LO isolation is beneficial. This helps minimize any leakage of the LO signal to the IF and RF, which could otherwise impact the quality of the signal. Ensuring proper LO isolation helps maintain signal integrity and enhances the overall performance of the mixer.

By carefully considering these factors, the most suitable mixer can be selected to meet the specific requirements of the application at hand. In the 1039nm laser system, we use a phase detector (ZRPD-1+) for PDH locking and a mixer (ZFM-2000) for FSR locking.

3.3.4 Photodetector

In order to accurately capture the reflected cavity signal at the modulation frequency $\Omega \sim 25$ MHz, it is crucial to employ a high-bandwidth photodiode. For our 918 nm laser, we have selected the New Focus 1801 photodetector, while for the 1039 nm laser, we utilize the New Focus 1811. These photodetectors are chosen for their fast response times and low noise characteristics. Additionally, we have implemented effective grounding techniques to minimize noise interference.

Additionally, to monitor the cavity transmission, we need a high-gain photodiode with low noise characteristics. For this purpose, we utilize the Thorlabs PDA36A high-gain photodetector, as the signal intensity after passing through the cavity is only a few μW. The high gain of this detector allows us to accurately measure and monitor the weak transmission signal from the cavity.

doi:10.6342/NTU202302912

3.3.5 Filter and Amplifier

Before turning on the amplifier, it is important to ensure that the output is properly terminated with a 50Ω load. Failure to do so can lead to potential damage to the amplifier.

In the setup, a band-pass filter is placed after the photodetector to prevent the direct amplification of the signal received by the detector. This is done to avoid amplifying all the noise generated by the detector itself within the bandwidth of the amplifier. By using a band-pass filter close to the modulation frequency, only the reflected signals of our main interest, such as the sidebands, can be amplified and fed into the mixer for demodulation.

On the other hand, a low-pass filter is employed to ensure that only lower frequency components of the output signal can enter the PID servo. The selection of the low-pass filter bandwidth is typically chosen to be slightly higher than the maximum feedback bandwidth of the servo.

In FSR locking, tunable bandpass filters (such as 5BT-1000/2000-1-N/N) are utilized to filter the frequency components from the mixer output at one of $\nu_{FSR} \pm \omega_2$. This filter is used to retain the differential frequency components, which are then employed as the local oscillator (LO) for demodulating the FSR error signal with high S/N.

3.4 Phase Lock to Laser Stabilization

The process of stabilizing the 1039 nm laser to the ULE cavity involves several steps. Initially, as depicted in Fig. 3.6 (a), the PZT is scanned at a rate of 10 Hz. The transmission peak corresponds to a resonant TEM_{00} mode, as confirmed by the CCD by reducing the scanning frequency and range. Adjust the HWP before the PBS to restrict reflected power

doi:10.6342/NTU202302912

and to fine-tune the error signal. If the power is too low, the S/N will be low, affecting the locking performance. On the other hand, if the power is too high, the photodiode will become saturated and the error signal will become distorted.

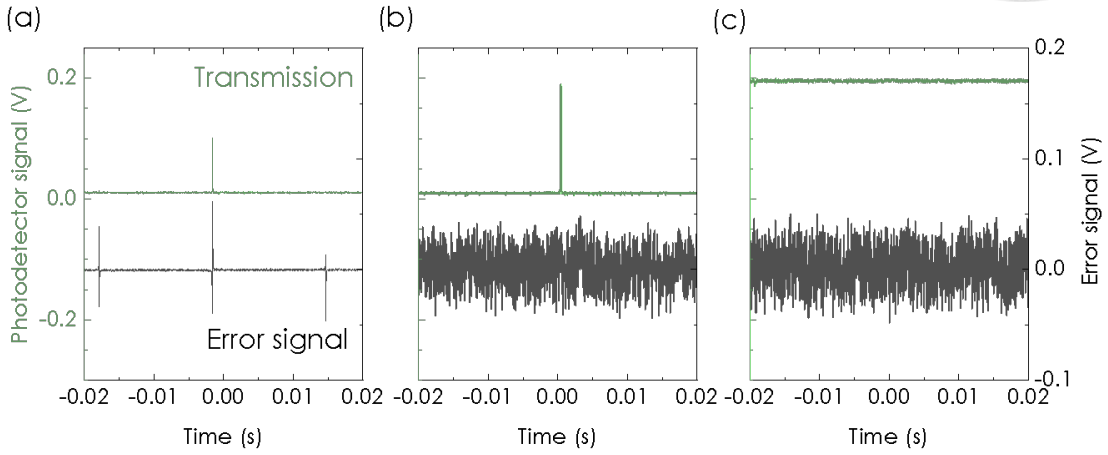

Figure 3.6: Cavity transmission signals of 1039nm laser with servo current loop (a) off and (b) on. (c) Laser initiates locking to cavity with PZT loop also enabled.

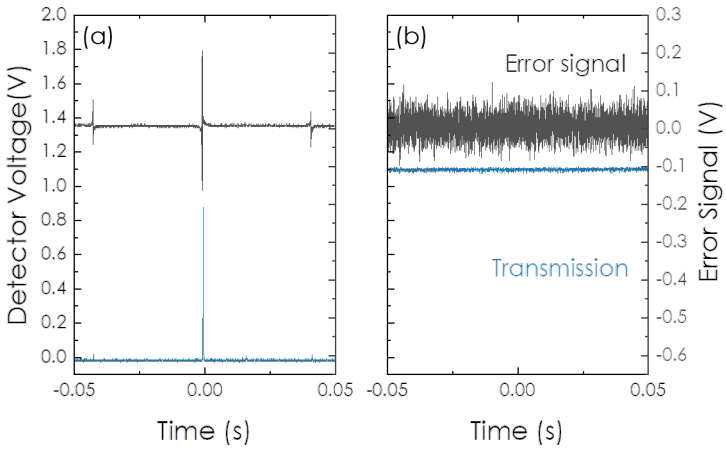

Figure 3.7: Cavity transmission signals of 918nm laser with both current and PZT servo loop (a) off and (b) on.

After preparing the error signal to be used as the input signal for the servo, the next step that needs to be taken is to adjust the input offset before moving on to change the gain. This offset adjustment is done to compensate for any background signals, ensuring that the lock level is positioned at zero. Frequency jitter near the cavity resonance is quickly compensated by the fast current loop feedback. This behavior is depicted in Fig.

doi:10.6342/NTU202302912

3.6 (b), where it can be observed that the fast current loop increases the amplitude of the transmitted peak.

We utilize the Toptica mFALC 110 and FALC pro as the fast laser locking servos for the 1039nm and 918nm lasers, respectively. These servo designs lack a P gain component, but include multiple I gain components that influence low-frequency behavior and D gain components that influence high-frequency behavior. Each of these gains corresponds to a different switch, which in turn affects the transfer function. By utilizing various combinations of these switches, we can effectively adjust the I and D gains to achieve the desired outcome.

Next, let's discuss how to adjust the servo of the current loop. Firstly, it is important to confirm whether the slope of the error signal at the resonance point is correct. To begin, all I and D gains are turned off, and the overall main gain of the servo is gradually increased. As the slope becomes steeper, indicating that the error signal is out of phase, the phase shifter needs to add or subtract 180°. This adjustment results in a flatter slope.

Following that, the I gain is fine-tuned to ensure the error signal remains locked at the resonant frequency for a short duration. This adjustment leads to a broadening of the transmission peak. Subsequently, the scanning range of the PZT is gradually reduced until the scanning operation completely stops. During this process, it is crucial to maintain the error signal locked at the desired lock point through the feedback provided by the current loop.

After fine-tuning the I gain, the subsequent step involves optimizing the D gain. The D gain plays a crucial role in providing feedback for higher-frequency phase noise. To optimize the D gain, a spectrum analyzer is utilized to analyze the servo bump. The D

doi:10.6342/NTU202302912

gain is adjusted iteratively until the frequency at which the servo bump occurs reaches its maximum value. This derivative action enhances the system ability to anticipate and respond to rapid changes in the error signal. Adjusting the D gain makes the controller more sensitive to these changes, enabling it to provide a faster corrective action and reduce the error between the reference signal and the system output. It is important to carefully tune the PID parameters, as excessively high gains can lead to instability and oscillations in the control system.

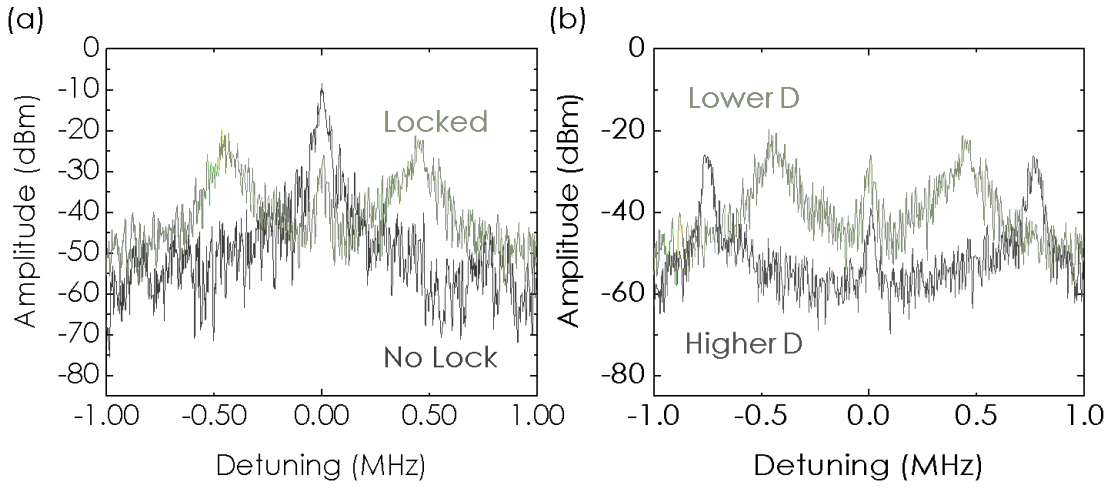

Figure 3.8: The error signal beat note, measured from the photodiode, exhibits a servo bump, indicating the bandwidth of the servo loop.

3.4.1 Servo Bump

Servo bumps are characteristic peaks or bumps in the spectrum that can affect the servo bandwidth due to the instability of the servo, as discussed in Sec. 2.1.2. To diagnose the servo bump, a portion of the error signal power is extracted prior to demodulation by the mixer. This extracted signal is then fed into a spectrum analyzer, with the center frequency set at the PDH frequency. The resulting spectrum, shown in Fig. 3.8, provides information about the locking bandwidth based on the noise peak. Additionally, when the gains are set too high, the spectrum analyzer may show an increase in peak height or the

doi:10.6342/NTU202302912

appearance of additional frequency oscillations, indicating excessive gains.

3.5 Measurement of Cavity Characterization

3.5.1 Cavity Ring-Down Signal

To determine the cavity finesse, one method is to scan the laser frequency and observe the corresponding changes in the transmitted light. From the transmitted light, one can obtain the ratio of the FSR to the cavity linewidth, which gives the cavity finesse, $\mathcal{F} = \nu_{\text{FSR}}/\delta\nu_{\text{cav}}$. However, in high-finesse cavities, photons can have longer lifetimes, and the cavity linewidth can be narrower than the laser linewidth. Therefore, it is necessary to directly measure the cavity decay time to accurately determine the finesse.

A method to measure the cavity decay time is by utilizing an AOM or EOM as a switch. However, if an optical path with an active switch is not required, using this method for measurement can be somewhat cumbersome. In 1997, Poirson proposed a simpler method to measure the cavity decay time [17]. When the laser frequency sweeps across the cavity resonance, the light undergoes multiple reflections between the two mirrors, with a portion of the light transmitting through the mirrors each time. By monitoring the final transmission of the light, the time it takes for the transmitted intensity to decay to 1/e can be determined, which corresponds to the cavity decay time. To obtain the cavity decay curve, the laser frequency or the length of the cavity can be scanned, and the scan speed can also impact the shape of the transmission curve. The cavity finesse can be determined by observing the changes in the I_1/I_2 ratio using the relationship defined in

$$2\pi\nu_{FSR}\Delta t = \frac{\mathcal{F}}{2}\left(\frac{I_1}{I_2} + 2 - e\right). \tag{3.6}$$

doi:10.6342/NTU202302912

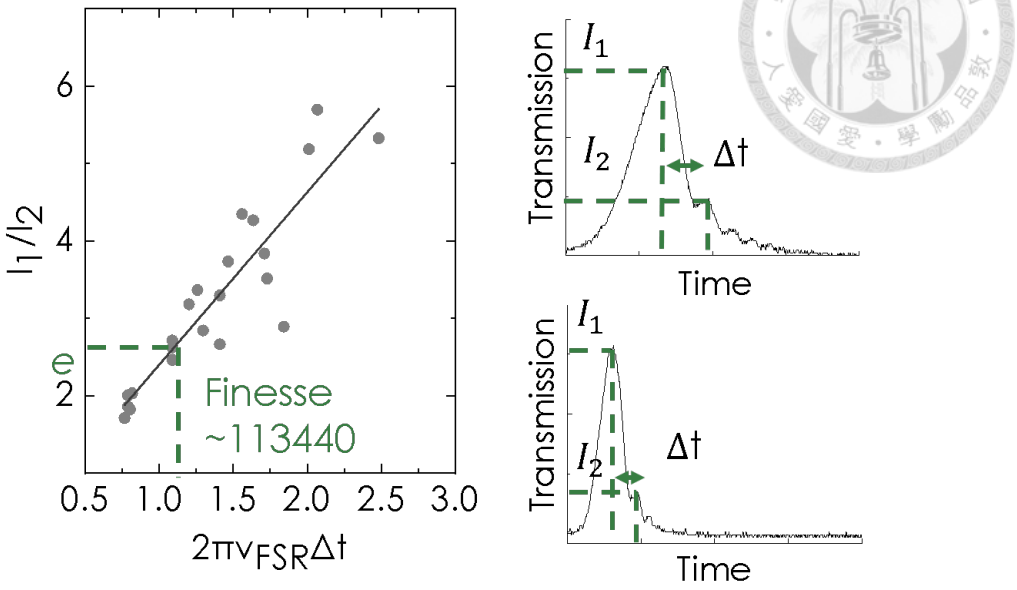

Figure 3.9: Measurement of the ringing effects in a Fabry-Perot cavity. (a) The finesse can be determined by the ratio I_1/I_2, which equals e. The transmitted intensity curves for different laser scanning frequencies are shown in (b) at 30Hz and (c) at 25Hz.

When the ratio of the first peak and the second peak is approximately e in Fig. 3.9 (a), we can estimate the cavity finesse to be around 113440. The transmitted intensity output is illustrated in Fig. 3.9 (b) for a laser scanning frequency of 30 Hz (c) 25 Hz.

3.5.2 FSR Locking

DeVoe and Brewer proposed the dual frequency modulation (DFM) technique in 1984 [18] to generate an error signal for locking the modulation frequency to the cavity FSR.

This method is similar to the PDH locking technique, where modulation is applied to the fiber-EOM and the error signal is obtained through demodulation. PDH provides the foundation for laser frequency stabilization, while FSR locking allows providing feedback to the piezo element of an Etalon or Fabry-Perot cavity, and these two techniques

doi:10.6342/NTU202302912

can be combined. As a result, the utilization of dual frequency modulation (DFM) is necessary, similar to the frequency sideband locking technique discussed in Sec. 2.4.3. In the following, we will provide a detailed explanation of the DFM process.

3.5.2.1 Dual Frequency Modulation (DFM)

When an incident light with an angular frequency of ω_0 is modulated at two frequencies, ω_1 and ω_2, the electric field entering the cavity can be represented using Fourier decomposition with Eq. 2.16.

$$\begin{aligned} E_{inc} &= E_0 e^{(i\omega_0 t + i\beta_1 sin\omega_1 t + i\beta_2 sin\omega_2 t)} \\ &\sim E_0 e^{i\omega_0 t}[J_0(\beta_1) + J_1(\beta_1)2isin\omega_1 t][J_0(\beta_2) + J_1(\beta_2)2isin\omega_2 t] \end{aligned} \tag{3.7}$$

To simplify the analysis, let's assume that the initial phases are set to 0. Here, ω_1 and ω_2 represent the RF frequencies close to the FSR of the cavity and the PDH modulation, respectively. β_1 and β_2 are the modulation indices for these frequencies, respectively, assuming they are both much smaller than 1. In this case, we can focus on the carrier and the first-order sidebands in the modulated signal. The incident light can be rewritten as follows:

$$\begin{aligned} E_{inc} = E_0 e^{i\omega_0 t}[&J_0(\beta_1)J_0(\beta_2) + J_0(\beta_1)J_1(\beta_2)2isin\omega_2 t \\ &+ J_1(\beta_1)J_0(\beta_2)(e^{i\omega_1 t} - e^{-i\omega_1 t}) \\ &+ J_1(\beta_1)J_1(\beta_2)e^{i\omega_1 t}2isini\omega_2 t \\ &- J_1(\beta_1)J_1(\beta_2)e^{-\omega_1 t}2isin\omega_2 t]. \end{aligned} \tag{3.8}$$

doi:10.6342/NTU202302912

The lineshape function of the cavity is a Lorentzian

$$g(\Delta) = \frac{\Delta(\Delta - i\Gamma)}{\sqrt{R}(\Delta^2 + \Gamma^2)}. \tag{3.9}$$

The reflected light can be represented as $E_{refl} = g(\Delta)E_{inc}$, assuming that ω_2 is greater than the cavity linewidth. Thus, $\omega_0 \pm \omega_2$ and $\omega_0 \pm \omega_1 \pm \omega_2$ will all be reflected with $g = 1$ when ω_0 is close to the cavity resonance. The RF detuning is denoted as $\delta = \omega_1 - \nu_{FSR}$ and the optical detuning as $\Delta = \omega_0 - n\nu_{FSR}$. Therefore, the reflected electric field can be expressed as:

$$\begin{aligned} E_{refl} = E_0 e^{i\omega_0 t}\{&J_0(\beta_1)J_0(\beta_2)g(\Delta) + 2iJ_0(\beta_1)J_1(\beta_2)sin\omega_2 t \\ &+ e^{i\omega_1 t}[J_1(\beta_1)J_0(\beta_2)g(\Delta+\delta) + 2iJ_1(\beta_1)J_1(\beta_2)sin\omega_2 t] \\ &- e^{-i\omega_1 t}[J_1(\beta_1)J_0(\beta_2)g(\Delta-\delta) + 2iJ_1(\beta_1)J_1(\beta_2)sin\omega_2 t]\}. \end{aligned} \tag{3.10}$$

3.5.2.2 Demodulation

The extracted detector heterodyne beat signal at $\omega_1 \pm \omega_2$ is

$$\begin{aligned} E_{refl}E^*_{refl}(\omega_1 \pm \omega_2) = &4|E_0|^2 J_0(\beta_1)J_1(\beta_1)J_0(\beta_2)J_1(\beta_2)sin\omega_2 t \\ &\times \{Im[g(\Delta+\delta) - g(\Delta-\delta)]cos\omega_1 t \\ &+ Re[g(\Delta+\delta) + g(\Delta-\delta) - 2g(\Delta)]sin\omega_1 t\} \end{aligned} \tag{3.11}$$

The coefficient of $sin\omega_1 t$ is 0, indicating that it does not contribute to the DFM signal. However, the $cos\omega_1 t$ term plays a role in the DFM signal. It is directly proportional to the difference in the cavity phase shifts of the $\omega_0 \pm \omega_1$ sidebands. The error signal can be

doi:10.6342/NTU202302912

made simpler with the Lorentzian line-shape function to

$$E_{refl}E^{*}_{refl}(\omega_1 \pm \omega_2) = -4|E_0|^2 J_0(\beta_1)J_1(\beta_1)J_0(\beta_2)J_1(\beta_2) \times \frac{\delta}{\Gamma}[sin(\omega_1+\omega_2)t + sin(\omega_1-\omega_2)t]. \tag{3.12}$$

The error signal remains unaffected by optical frequency jitter. Furthermore, when $\beta_1 = \beta_2 = 1$, the expression

$$4J_0(\beta_1)J_1(\beta_1)J_0(\beta_2)J_1(\beta_2) = 0.45. \tag{3.13}$$

indicates an excellent signal-to-noise ratio.

3.5.2.3 Setup

The experimental setup, depicted in Fig. 3.10, is built upon the 1039nm laser system. To introduce an additional modulation frequency close to the cavity FSR, we employ a signal generator (Agilent E4435B) to generate a modulation frequency of approximately 1.4966GHz. This specific frequency value, obtained through manual scanning of the cavity linewidth, will be discussed in detail in Sec. 3.5.3. The signal source can also be replaced with a voltage-controlled oscillator (VCO). The FSR frequency and the PDH frequency are combined using a power splitter (ZFSC-2-1+), and the resulting combined signal is fed into a fiber-EOM for modulation.

The setup for FSR locking is similar to PDH locking in that it requires the detection of reflected light. We utilize the Thorlabs APD310 photodetector, which has a bandwidth of up to 1600MHz, to receive the FSR frequency signal. However, if we were to use this detector for both FSR locking and PDH locking simultaneously, the error signal would be susceptible to higher-frequency noise, leading to a compromised signal-to-noise ratio

doi:10.6342/NTU202302912

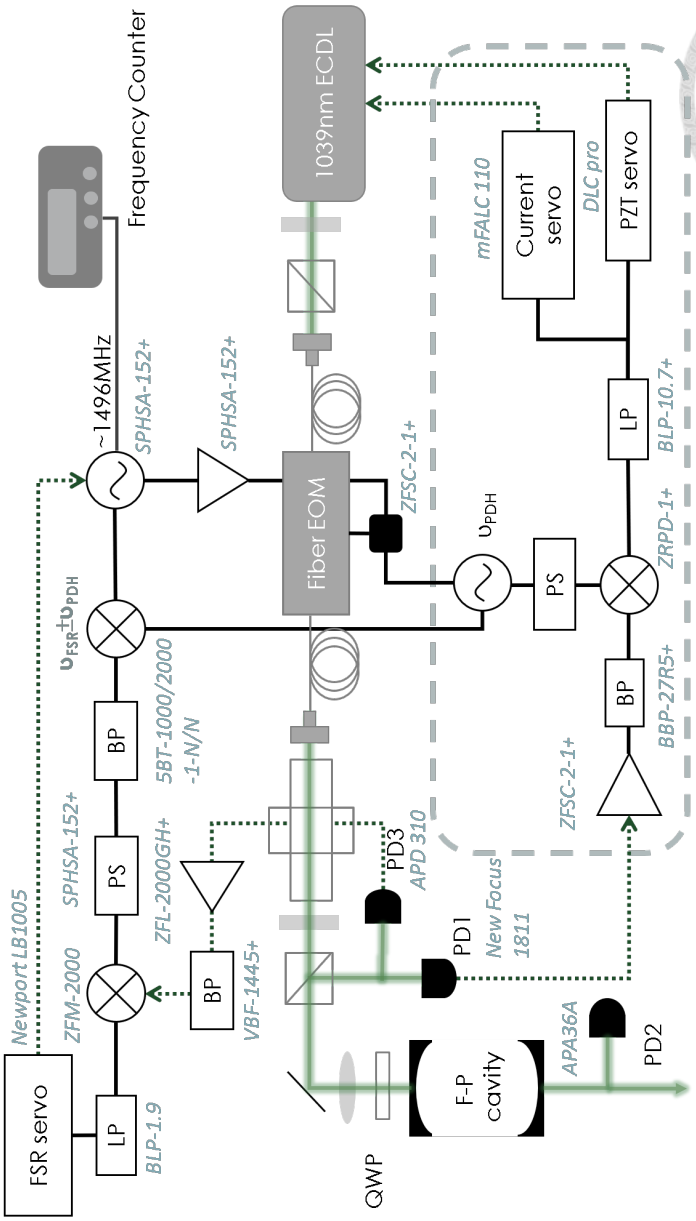

Figure 3.10: PDH and FSR locking configuration for 1039nm laser.

compared to using a Newport detector with a narrower bandwidth of 125MHz. Therefore, we have opted to use two detectors to maintain better laser locking performance.

For FSR locking, the demodulation frequency utilizes one of $\omega_1 \pm \omega_2$. We have chosen to demodulate the frequency $\omega_1 - \omega_2$, and thus it is necessary to generate the sum and difference frequencies of the PDH frequency and FSR frequency using a mixer. The mixer we use in this setup does not require a DC output. Subsequently, a band-pass filter is employed to allow only the desired difference frequency $\omega_1 - \omega_2$ to pass through. The

doi:10.6342/NTU202302912

selection and limitations of other RF components align with Sec. 3.3.

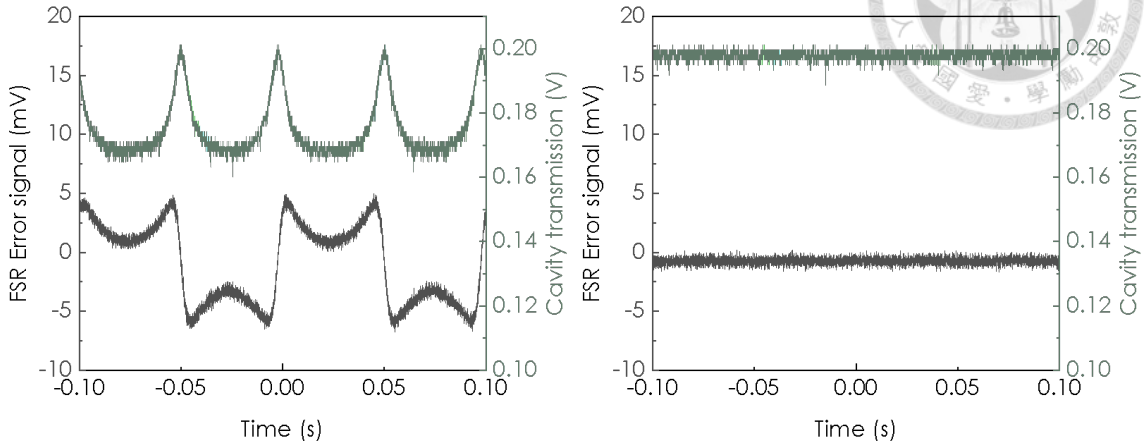

Figure 3.11: The error signal obtained from FSR locking and the cavity transmission signal can be observed by scanning the signal generator (a) and when locked at FSR (b).

The FSR signal source, operating at a frequency close to the cavity FSR with a scanning frequency of 10 Hz and a frequency range of 50 kHz, generates an error signal after demodulation, as depicted in Fig. 3.11 (a). The zero crossing of the error signal corresponds to the FSR. In Fig. 3.11 (b), it can be observed that the FSR signal is locked to a specific output frequency. At this frequency, both the carrier and the sidebands at ω_1 are able to pass through the cavity, leading to a sustained maximum transmission intensity.

The value of FSR can be measured using a frequency counter, but the accuracy of the frequency reading is influenced by the gatetime of the frequency counter (Keysight 53220A). In our experimental setup, we ensured that the servo gain and phase shift remained unchanged to avoid altering the lock level of the FSR error signal. We employed external frequency modulation to lock the FSR value to the output frequency of the RF function generator. The gatetime of the frequency counter was set to 500 ms. We recorded the FSR value four times, with each recording lasting for 2 minutes, for a total duration of 20 minutes. By choosing these recording parameters, we made the assumption that the measurement fluctuations would be much larger than any actual FSR drift. Fig. 3.12 dis-

doi:10.6342/NTU202302912

plays the recorded FSR values obtained as we adjusted the lock level of the PDH-locked laser. It is evident from the results that the RF frequency locked at the FSR exhibited slight

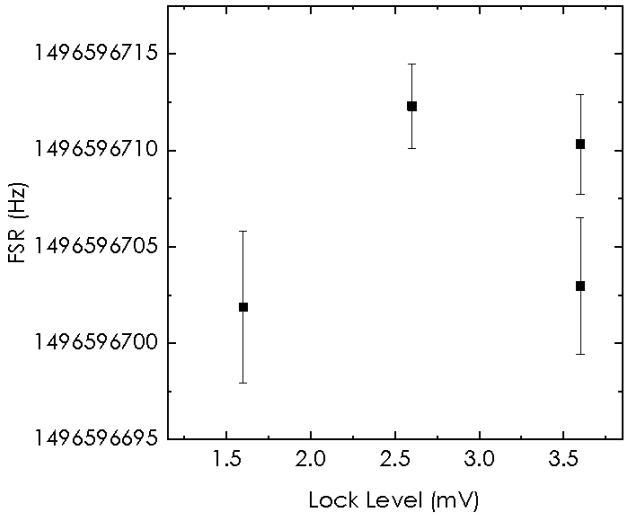

Figure 3.12: The frequency counter reads the output frequency of the signal generator, which is locked to the FSR, with slight variations in the laser lock level.

center frequency shifts of a few Hz, while the frequency fluctuations remained relatively consistent. Consequently, in our FSR locking system, when adjusting the laser lock level within a range of 20 mV, the average FSR at a wavelength of 1039.236 nm was determined to be 1496596707 ± 6.299 Hz at that time.

3.5.3 Cavity Linewidth

As mentioned earlier in Sec. 3.5.2, automatic feedback is employed to lock RF modulation signals and determine the FSR. However, the measurement results of the FSR locking method are influenced by the servo feedback control. In our system, when making adjustments to the phase shifter, an offset is introduced and shifts the input signal. It is necessary to compensate for this offset to align the background level with the zero point of the error signal. However, adjusting the offset and fine-tuning the servo gain may also

doi:10.6342/NTU202302912

affect the accuracy of the FSR measurement. Therefore, FSR locking might not be the most efficient approach when only a few measurements are required. In such cases, alternative methods or strategies may need to be considered to achieve efficient and accurate FSR measurements.

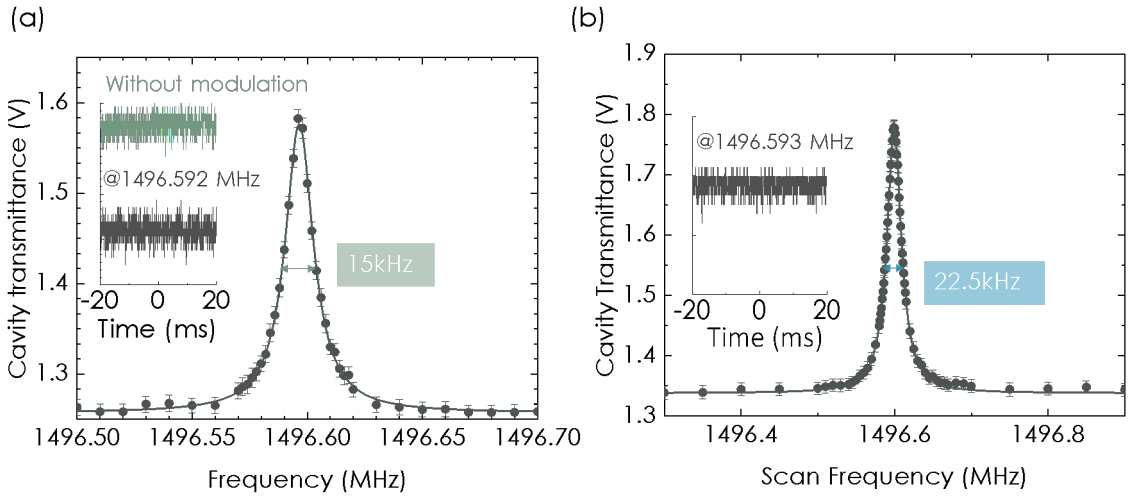

Figure 3.13: The cavity linewidth is measured by employing DFM and manually scanning the frequency near resonance to determine the FSR using both the 1039nm (a) and 918nm (b) lasers.

Indeed, the concept of this method is similar to the FSR locking concept, as both are based on dual frequency modulation. The main difference is that in FSR locking, the frequency scanning is performed using a function generator, while in this method, it is done manually. During the laser locking process, when the additional modulation frequency ω_1 is adjusted, it leads to a decrease in the power of the carrier. However, when ω_1 is tuned close to the FSR frequency, the transmitted intensity exhibits variations as the scanning frequency sweeps within the cavity linewidth. This behavior is depicted in Fig. 3.13. The transmitted optical intensity follows a Lorentzian profile. Since the laser linewidth is much narrower than the cavity linewidth in this case, the F-P cavity linewidth and FSR can be determined [19]. With these values, the finesse of the cavity can be calculated. Table 3.1 shows that the reflectivity of the mirror coatings varies for different wavelengths, resulting

doi:10.6342/NTU202302912

in different finesse values.

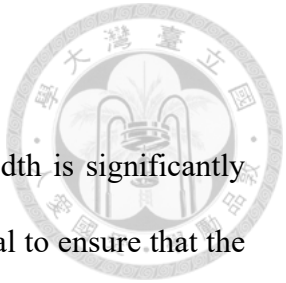

However, this method is only applicable when the laser linewidth is significantly smaller than the cavity linewidth ($\delta\nu_L \ll \delta\nu_C$). Therefore, it is crucial to ensure that the laser is properly locked to the cavity resonance and exhibits good locking performance.

Wavelength	Cavity Linewidth	FSR	Finesse
1039.2365nm	14.917±0.206kHz	1496596511±58Hz	100288.26±1385.51
918.8972nm	22.560±0.140kHz	1496599400±38Hz	66338.63±411.68

Table 3.1: The results of our F-P cavity characterization using DFM with manual scanning of ω_1 are shown in Fig. 3.13. The data points are fitted with a Lorentzian function to obtain the cavity linewidth.

3.6 Laser Characterization

3.6.1 Laser Linewidth

A commonly used method for measuring laser linewidth is self-heterodyne detection combined with a Mach-Zehnder interferometer, as shown in Fig. 3.14 (a). This method is preferred for achieving high measurement precision among the multiple methods available for linewidth measurement. In this method, the optical phase or frequency fluctuations are converted into intensity variations by modulating the frequency on the long arm of the interferometer. The linewidth is determined by measuring the beat signal obtained on a spectrum analyzer. However, in order to eliminate any residual phase correlation between the arms of the interferometer, the delay length of the fiber must be longer than the coherence length of the laser. This requirement can lead to long delay lengths, sometimes spanning several kilometers, especially when the laser linewidth is narrow.

doi:10.6342/NTU202302912

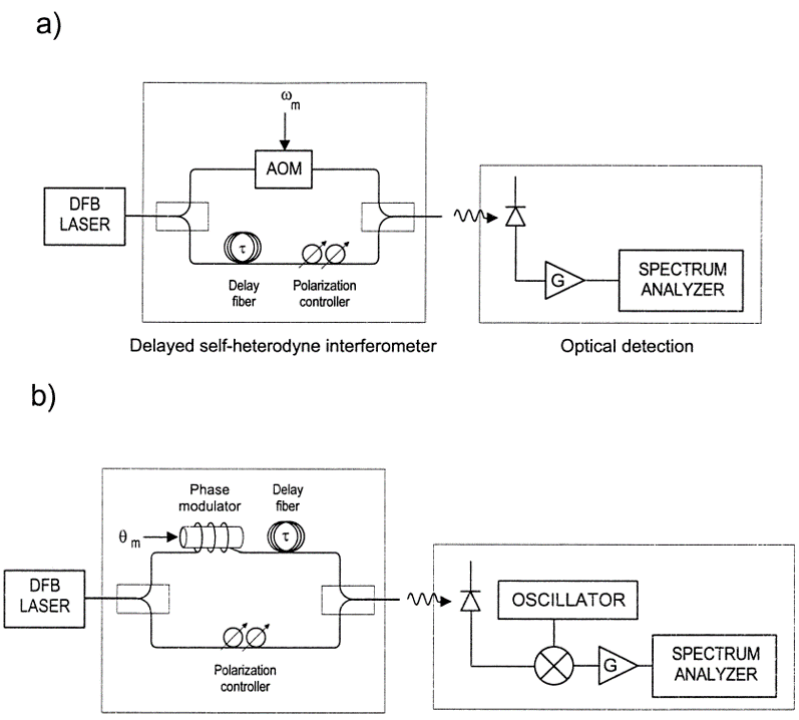

Figure 3.14: Setups for measuring laser linewidth. (a) Self-heterodyne configuration; (b) Self-homodyne configuration. Taken from [20].

In Fig. 3.14 (b), an improved method for measuring laser linewidth is self-homodyne detection. In this method, the phase modulation is performed on the long arm of the interferometer, and an additional RF or microwave mixer is added to obtain the linewidth measurement. However, it is important to note that to ensure accuracy in laser linewidth measurement, the length of the delay fiber also needs to be properly chosen.

Another method for accurate laser linewidth measurement is to use a stable reference laser of the same wavelength. However, due to the constraints of our laboratory equipment, we have not been able to employ these methods for precise linewidth measurement. Instead, we rely on rough estimates of laser frequency fluctuations by analyzing the intensity fluctuations of the transmitted light. Although this approach does not yield a direct measurement of the linewidth, it allows us to make a rough assessment of the laser frequency variations by monitoring changes in the intensity of the transmitted light. Based on the measurement results presented in Sec. 3.5.3, where it was determined that the laser

doi:10.6342/NTU202302912

linewidth is narrower than the cavity linewidth, we assume a coupling efficiency of 1 for the carrier laser light into the cavity [21]. Therefore, we employ a rough estimation method based on the relationship between the intensity variation of the transmitted light and the laser scanning frequency, utilizing the measured data of the F-P cavity linewidth shown in Fig. 3.13. This estimation method enables us to approximate the variations in the laser frequency by observing the changes in the transmitted light intensity.

The frequency fluctuation can be estimated within the Lorentzian fitting of the cavity linewidth by adjusting ω_1 in the DFM to the frequency where the slope shows the largest change. Frequency fluctuations at 1039 nm and 918 nm lasers are roughly 350 Hz and 621 Hz in 40 ms, respectively, as shown in Fig. 3.13.

3.6.2 Laser Stability

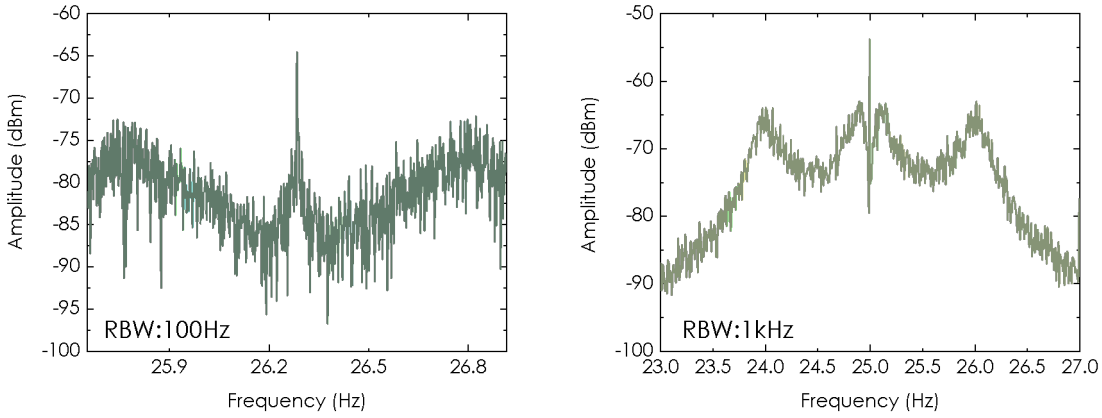

Figure 3.15: The error signal beat note exhibits a servo bump, which provides information about the bandwidth of the servo loop at 1039nm (a) and 918nm (b).

In the final locking performance, as observed in the in-loop photodetector RF spectrum signals in Fig. 3.15, servo bumps are clearly visible at 1 MHz and 760 kHz for the 918 nm and 1039 nm lasers, respectively. These bumps indicate the bandwidth of the fast current feedback. In diode lasers, phase noise at low frequencies contributes significantly

doi:10.6342/NTU202302912

to linewidth broadening [20]. Therefore, the high feedback bandwidth in our system effectively suppresses low-frequency phase noise. The frequency fluctuations of the 459 nm laser are twice that of the 918 nm master laser.

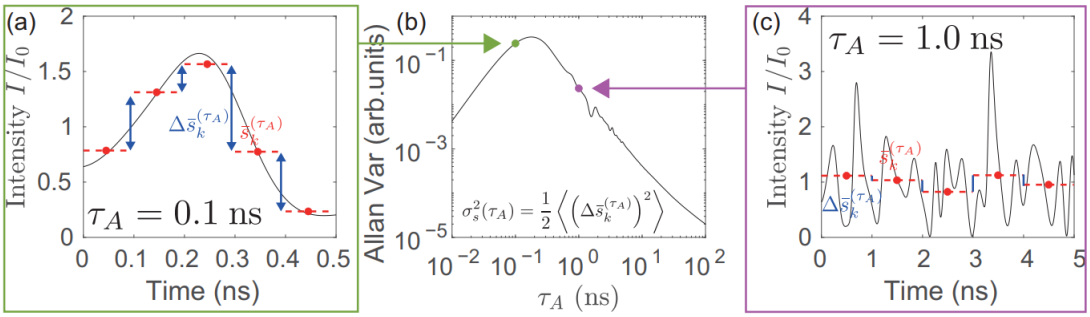

Figure 3.16: The Allan variance analysis is applied to a laser time series with τ_A ranging from 10^{-2} to 10^{2} ns. The green and purple dots represent the Allan variance when τ_A is (a) 0.1 ns and (c) 1.0 ns, respectively. Taken from [22].

The Allan variance of a time series $s(t)$ provides insights into the variation or instability over time, and it is defined using the variance of $\Delta\bar{s}_k^{(\tau_A)}$ as [22]

$$\sigma^2(\tau_A) = \frac{1}{2}\left\langle \left(\Delta\bar{s}_k^{(\tau_A)}\right)^2 \right\rangle. \tag{3.14}$$

Where

$$\Delta\bar{s}_k^{(\tau_A)} = \bar{s}_k^{(\tau_A)} - \bar{s}_{k-1}^{(\tau_A)} \tag{3.15}$$

and

$$\bar{s}_k^{(\tau_A)} = \frac{1}{\tau_A}\int_{t_k}^{t_{k+1}} s(t)dt. \tag{3.16}$$

The quantity $\Delta\bar{s}_k^{(\tau_A)}$ is represented by the blue arrows in the examples shown in Fig. 3.16 (a) and (c). Here, $t_{k+1} = t_k + \tau_A$. Fig. 3.16 (b) displays the Allan variance analysis for different τ_A. This method allows obtaining the Allan variance using laser intensity time series instead of a phase time series.

We measured and recorded the variations in laser light intensity using a Rohde &

doi:10.6342/NTU202302912

Schwarz RTO2000 oscilloscope, as shown in Fig. 3.13. The measurements were taken over a record time of 40ms, with sample rates set at 100kHz for the 1039nm laser and 50kHz for the 918nm laser. The time series data is utilized to calculate the Allan variance using Eq. 3.14. The frequency uncertainty is calculated by evaluating the variation in transmission intensity going through the cavity, as shown in Fig. 3.17. This analysis provides information about the laser linewidth, which is narrowed down to 1kHz with an integration time of 1ms for the 1039nm laser and 0.1ms for the 918nm laser. The cavity Lorentzian spectral line form is used for voltage-to-frequency conversion.

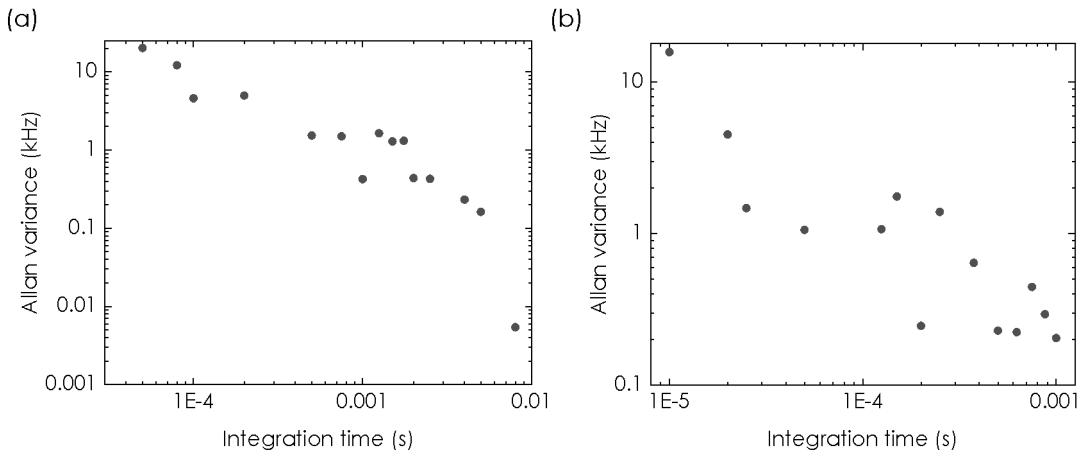

Figure 3.17: The Allan variance of the laser frequency relative to the cavity resonance is shown for the 1039nm laser in (a) and the 918nm laser in (b). Both axes are in logarithmic scale.

doi:10.6342/NTU202302912

Chapter 4

Lasers for Rydberg Excitation

To suppress the phase noise of the lasers and minimize the influence of laser frequency fluctuations on Rydberg excitation, we lock both lasers to an additional high-finesse resonator. However, since the frequency used to excite atoms to the Rydberg state is different from the resonant frequency of the cavity, we need to employ other methods to adjust the frequency of the 1039 nm laser. As mentioned earlier in Sec. 3.2.1, it is important to avoid high laser power to prevent thermal shifts in the cavity resonant frequency. However, this low power transmission through the cavity makes it challenging to directly use the transmitted light for excitation. In order to achieve high power at the desired frequency for atom excitation, we use diode injection locking as the seed of a fiber amplifier.

Additionally, although the ULE cavity helps to mitigate the impact of environmental temperature fluctuations, it still experiences long-term frequency drift. To establish a frequency reference, we employ Doppler-free saturation spectroscopy. This technique allows us to measure the frequency drift at different cavity temperatures and select the temperature at which the long-term frequency drift is minimized.

doi:10.6342/NTU202302912

4.1 Cavity Filtering

In PDH frequency locking, the finite bandwidth of the feedback loop introduces the servo bump, which can be considered a form of noise. However, due to the high finesse of the optical cavity, it acts as an optical frequency filter, allowing only frequencies within the cavity linewidth to pass through. Hence, the light transmitted through the cavity effectively filters out the influence of the servo bump, preserving only the narrow linewidth laser with reduced phase noise. This characteristic makes the optical cavity an important component for reducing noise and improving locking stability. Additionally, besides eliminating the servo bump, the cavity also helps in eliminating other sources of noise, such as environmental vibrations and instability in the light source, thereby providing a cleaner and more stable output beam.

4.1.1 Injection Lock

Laser injection locking is a technique used to achieve high power output by injecting a weak, low-noise, low-power master laser (or seed laser) into the resonant cavity of a second diode laser, referred to as the slave laser. By adjusting the temperature and current of the slave laser, and ensuring that the frequencies of the master laser and the free-running slave laser are sufficiently close, the injection forces the slave laser to operate precisely at the injected frequency. The higher the injection power, the larger the allowable frequency offset between the master laser and the slave laser. Through injection locking, the master laser captures and controls the oscillating behavior of the free-running slave laser, ensuring that it operates precisely at the injected frequency. This process leads to a high power output with reduced noise. The experimental setup is illustrated in Fig. 4.1. We utilize a

doi:10.6342/NTU202302912

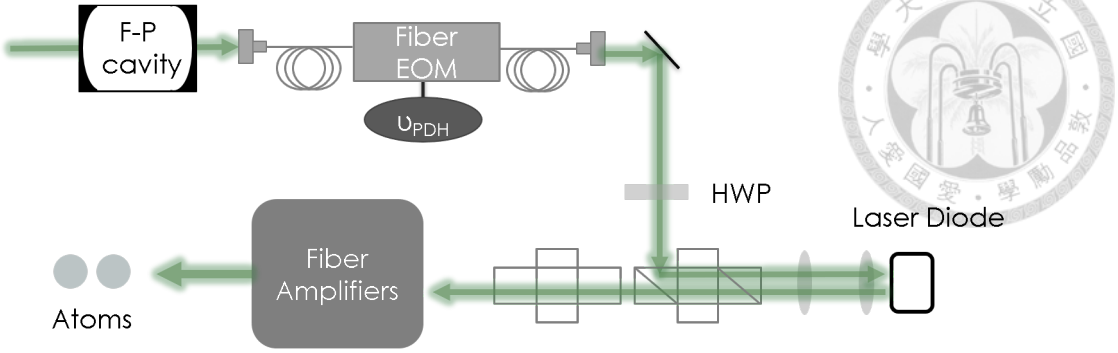

Figure 4.1: A diode is injected by sending a seed laser, which is a frequency-stabilized laser passing through a fiber-EOM to modulate the +1 or -1 sideband. The injection-locked laser then serves as the seed for fiber amplification, allowing for high-power laser generation with outputs reaching up to 50W.

low-power transmitted light at 1039 nm, with an approximate power of 500 μW, obtained from an ECDL locked to a cavity using the PDH technique. This transmitted light is modulated using a fiber-EOM to generate sidebands. To prevent both the carrier frequency and sideband frequencies from being injected into the slave laser simultaneously, we utilize an additional scanning Fabry-Pérot cavity. This cavity helps optimize the modulation depth, enabling the sideband power to exceed the carrier power significantly. As a result, we have the flexibility to choose either the +1 order or -1 order sideband frequency for injection into the slave laser, depending on our requirements.

In order to shape the light emitted by the diode laser, two cylindrical lenses are used, and the light is directed through an isolator coupled to both ends of a PBS. The master laser beam is reflected by the PBS at the rear end, directing it back towards the diode laser. A half-wave plate is used to adjust the polarization of the master laser beam, enabling efficient injection of the power into the diode laser. The output light from the injection-locked slave laser is characterized by its low-noise properties.

To prevent the instability caused by light reflecting back into the diode laser during subsequent experiments, we incorporate a second isolator. However, for the desired

doi:10.6342/NTU202302912

atomic applications, the laser output after injection locking becomes the seed laser for further amplification using a fiber amplifier. This amplification stage increases the power to 50W, allowing for efficient excitation with a large detuning in the intermediate state for Rydberg excitation.

4.2 Laser Calibration

The ULE glass used in the cavity has a vanishing first-order derivative term $\frac{d\nu}{dT}$ with respect to temperature, and the cavity is already placed in a vacuum environment, making it less sensitive to temperature fluctuations. However, it can still be affected by long-term heating when the laser is operational or by the influence of the final equilibrium temperature set by the temperature control system, leading to long-term resonant frequency drift. To mitigate significant frequency drift that would necessitate frequent recalibration of the laser to the atomic wavelength, our objective is to set the cavity at the zero-crossing temperature.

To determine the zero-crossing temperature, the commonly used approach is to measure the beatnote using a stable reference laser with a similar wavelength. However, in our case, we do not have another laser available with a comparable frequency. Therefore, we employ Doppler-free saturation spectroscopy [23], as described in Sec. 4.2.1.

This technique utilizes the 459nm laser in our Rydberg laser system, where the master laser at 918nm is locked to the cavity using PDH locking, as depicted in Fig. 4.5. The frequency difference between the crossover lines corresponding to the transitions from $6S_{1/2}$ F = 4 to $7P_{1/2}$ F' = 3 and F' = 4 is measured using the 459nm laser. This frequency difference provides us with the relative frequency drift of the 918nm laser with respect to

doi:10.6342/NTU202302912

the cavity resonance. By determining the zero-crossing temperature, we can mitigate the long-term frequency drift of the cavity.

4.2.1 Doppler-Free Saturation Spectroscopy

When a laser beam is directed into a vapor cell at room temperature, if the frequency of the laser light matches the transition frequency of the cesium atoms, the atoms will absorb the laser light. This absorption leads to a reduction in the power of the laser beam after passing through the cell. By analyzing the transmitted laser power, we can obtain an atomic absorption spectrum. The linewidth of this spectrum is typically very wide, reaching a few hundred megahertz. The broadening observed in the absorption spectrum, characterized by a Gaussian profile, is significantly larger than the intrinsic frequency width of an atomic transition. This broadening is mainly attributed to the Doppler effect, which arises from the thermal motion of atoms at room temperature.

From Fig. 4.2(a), it can be observed that when an atom at room temperature moves along the z-axis with a velocity V, and interacts with a laser beam propagating in the -z direction, the laser frequency observed by the moving atom is given by $f_{atom} = f_{probe}(1 + V_z/c)$. When the laser frequency is lower than the transition frequency f_0, it matches the resonant frequency for the moving atom. Conversely, if the atom is moving in the same direction as the laser beam, the laser frequency observed is given by $f_{atom} = f_{probe}(1 - V_z/c)$. As a result, the atom absorbs photons of higher frequencies.

When a pump beam, with higher power than the probe beam, propagates through the cell in the opposite direction, the probe beam experiences a redshift, while the pump beam experiences a blueshift, when interacting with atoms moving in the same direction as the

doi:10.6342/NTU202302912

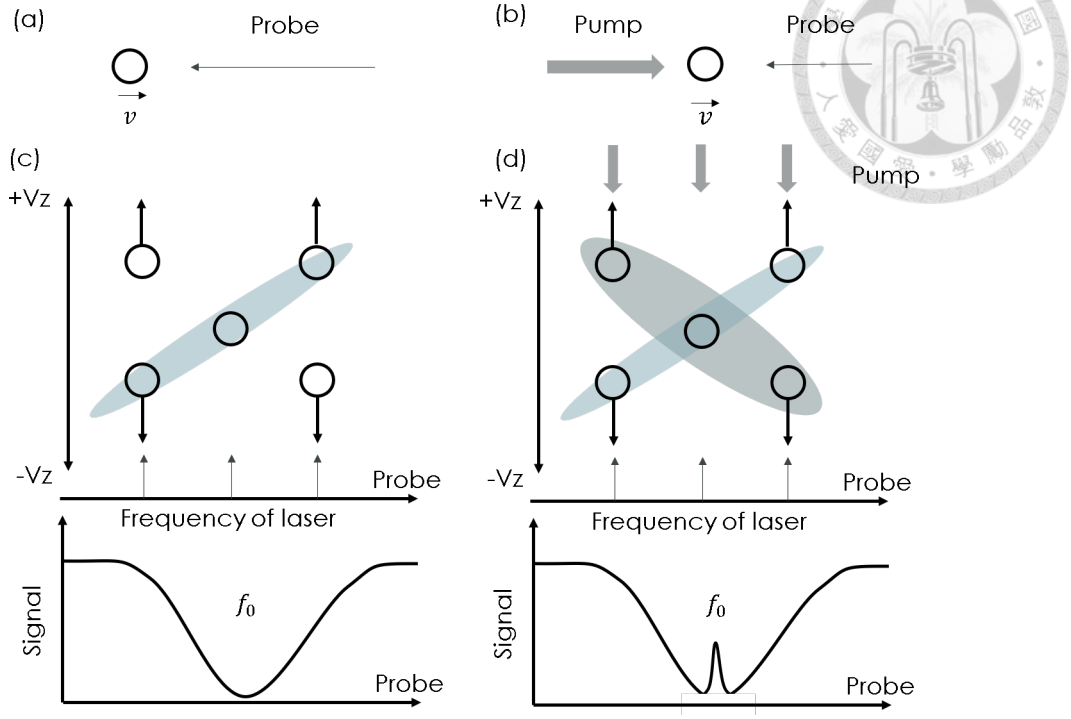

Figure 4.2: (a)(c) In absorption spectroscopy, when a probe beam is incident on an atom, atoms with a relative velocity experience the Doppler effect, and they perceive the probe beam's frequency to be exactly matching the atomic transition frequency. The absorption of photons by the atoms leads to a decrease in the transmitted intensity of the probe beam. (b)(d) In saturated absorption spectroscopy, another pump beam is counter-propagated with respect to the probe beam and is incident on the atoms. Atoms with zero relative velocity along the z-axis have already absorbed the pump beam, allowing the probe beam to pass through.

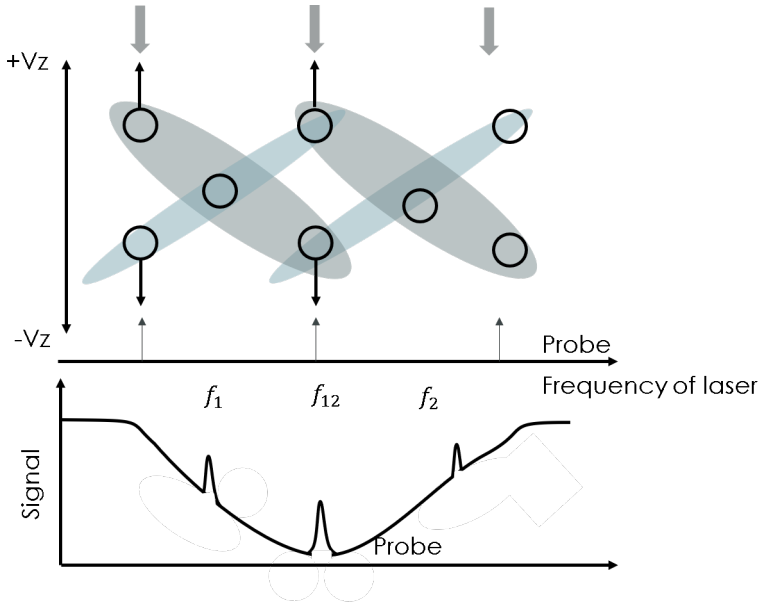

Figure 4.3: When scanning the laser frequency between two hyperfine levels, atoms from two velocity groups simultaneously absorb the pump beam, resulting in a crossover line.

doi:10.6342/NTU202302912

probe beam. As a result, atoms within the same velocity group do not simultaneously absorb the probe and pump beams. Only atoms with zero velocity in the z-direction, which absorb the pump beam, leading to a decrease in the population of ground state atoms, exhibit a reduction in the absorption rate of the probe beam, resulting in a spike in the spectrum, as shown in Fig. 4.2 (d).

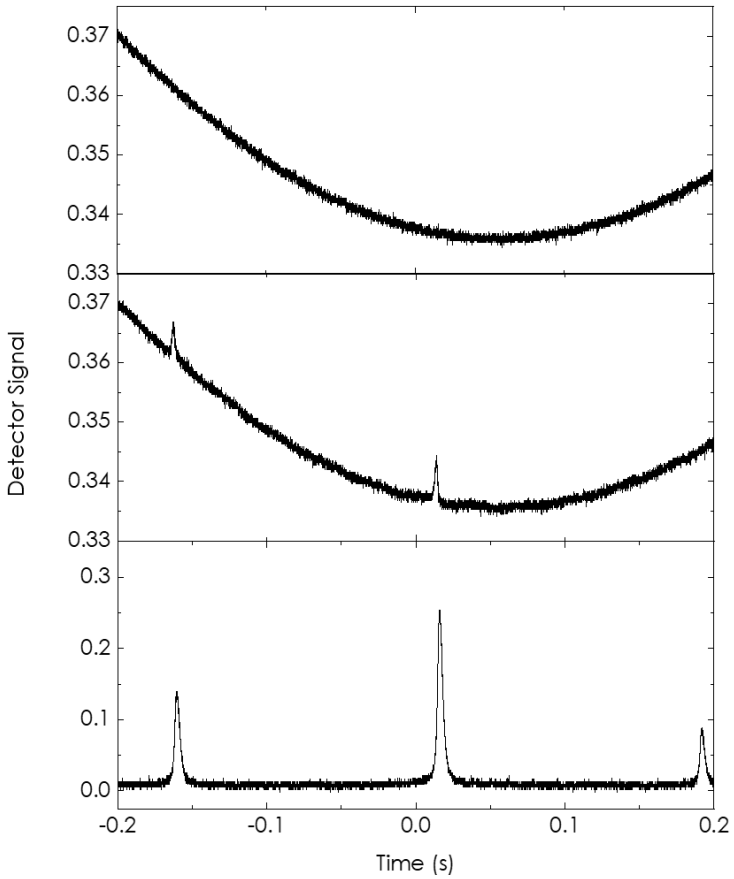

Figure 4.4: The probe transmission through the Cs cell exhibits (a) absorption spectrum, (b) saturated absorption spectrum, and (c) Doppler-free saturation spectroscopy.

When multiple hyperfine energy levels are present in an atomic system, the excitation of the system using a counter-propagating beam can result in the appearance of crossover

doi:10.6342/NTU202302912

lines. The presence of crossover lines is attributed to the interaction between moving atoms and the pump and probe beams. As depicted in the lower diagram of Fig. 4.3, each peak on the left and right represents a different transition frequency, while the peak in the middle corresponds to the crossover line. As depicted in the upper diagram, at the central frequency between the two transitions, two velocity groups of atoms are excited by the pump beam, leading to a reduction in the population of the ground state. Consequently, the intensity of the probe beam that is not absorbed becomes more pronounced. Crossover lines can exhibit higher intensities compared to the main saturation absorption peak and are often preferred for subsequent experimental studies.

4.2.2 Experiential Setup

In our experimental setup for saturated absorption spectroscopy with a 459 nm laser, the laser power is approximately 100 μW, which is generated from a SHG laser system capable of exciting Cs atoms from the $6S_{1/2}$ to $7P_{1/2}$ state. The experimental configuration is illustrated in Fig. 4.5. Initially, the laser beam is focused using a lens to achieve the desired beam size and shape. The beam is then split into two paths, and their respective intensities are adjusted using a combination of a PBS and a HWP. One path serves as the probe beam, which passes through the Cs cell directly. The other path is the pump beam, which is used to eliminate the Doppler broadening effect. While a common approach involves using a chopper to switch the pump beam on and off, we have chosen to employ an AOM to prevent the vibrations from the chopper that may affect the stability of the laser locking. By using the AOM, we ensure that the first-order diffracted light passing through the AOM exhibits maximum power and efficiency.

The probe and pump beams are combined and overlapped by passing through a PBS

doi:10.6342/NTU202302912

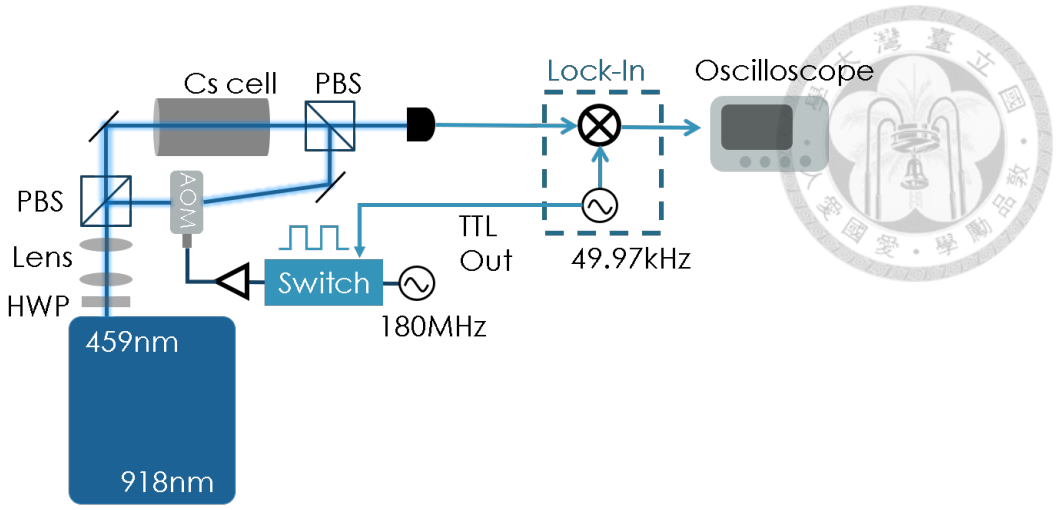

Figure 4.5: Setup for Doppler-free saturation spectroscopy utilizing AOM to switch the pump beam.

positioned after the Cs cell. To ensure excellent overlap of the optical paths, a BK7 glass element is placed before entering the cell. This helps align and overlap the probe beam and pump beam. To minimize the influence of environmental magnetic fields, we utilize a magnetic shielding material called soft ferromagnetic alloy sheets (Moxie FKR-120) that completely surrounds the cell, leaving only a small aperture for laser beam entry. To effectively shield against environmental magnetic fields, we have implemented a four-layer isolation setup, which provides magnetic field attenuation in the range of 20 to 30 dB for magnetic fields below 100 μT (1000 mG) at 50 Hz.

Due to the weak signal that is often hidden by the Doppler broadening background, a lock-in amplifier is employed to extract the signal. The TTL signal from the lock-in amplifier is utilized to control an AOM, acting as the frequency switch for the pump light. The time constant of the lock-in amplifier is set to 1 ms to minimize background noise, and the phase shift is adjusted to maximize the signal strength. The resulting Doppler-free saturation spectroscopy measurements are shown in Fig. 4.6. The transition from $6S_{1/2}$ to $7P_{1/2}$ has a natural linewidth of $2\pi \times 126$kHz as mentioned in the paper [24]. The linewidth obtained from the fitting of the signal to a Lorentian function, as shown in Table

doi:10.6342/NTU202302912

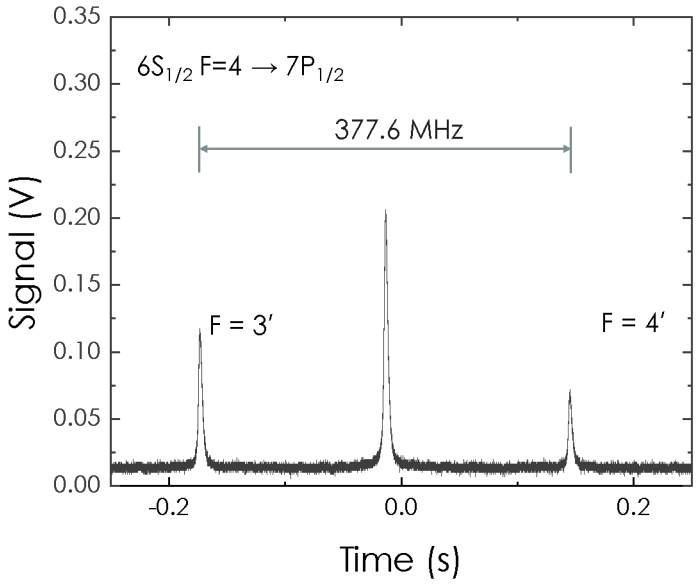

Figure 4.6: Hyperfine spectroscopy from the $6S_{1/2}$ F = 4 to the $7P_{1/2}$ state.

4.1, is approximately 4 MHz. This linewidth is broader than the natural linewidth of the transition, which is mentioned to be $2\pi\times$ 126 kHz. The broadening of the linewidth may be attributed to power broadening, which occurs when the transition is subjected to a high power level, resulting in an increase in linewidth.

Transition	Linewidth
F=4-3’	4.02MHz ± 3.08kHz
Crossover	4.06MHz ± 2.10kHz
F=4-4’	4.05MHz ± 4.22kHz

Table 4.1: The measurement result of the linewidth for the transition from $6S_{1/2}$ to $7P_{1/2}$

However, it should be noted that the measured probe light frequency used in the measurement process is shifted by the AOM. Therefore, the resonant frequency of the transition needs to take into account the frequency shift caused by the AOM. Let’s assume that the frequency of the crossover line for the $6S_{1/2}$–$7P_{1/2}$ transition is denoted as f_{atom}. The relationship between the 459nm laser frequency f_{459} and f_{atom} can be expressed as follows:

$$f_{459} = f_{atom} + \frac{1}{2} f_{AOM}. \tag{4.1}$$

doi:10.6342/NTU202302912

4.2.3 Long-Term Cavity Drift

In Sec. 2.4.3, it was explained that the 918nm laser employs the frequency offset locking technique to lock to one of the resonance frequencies of the cavity using DFM. By matching the +1 order sideband frequency to the cavity resonance, the relationship between the frequencies of the 918nm laser and the cavity can be expressed as:

$$f_{918} = f_{cavity} - f_{EOM}. \tag{4.2}$$

Since the 459nm laser is the second harmonic of the 918nm laser, we can combine Eq. 4.1 and Eq. 4.2 to establish the relationship between the atomic spectral line and the cavity resonance frequency. This relationship allows us to track the optical frequency drift and make necessary adjustments for maintaining the stability of the system.

From Fig. 4.11(a), it can be observed that at around 33.04°C, we typically wait for approximately 3 days after adjusting the cavity temperature controller before conducting measurements. This is because the cavity is in a vacuum environment, and it takes longer for the temperature to reach equilibrium. Once the temperature enters a stable drift range, we begin the measurements. On average, we perform measurements for more than 7 days to estimate the optical frequency drift at different temperatures. To adjust the frequency of the 918nm laser locked to the cavity, we manually sweep the modulation offset frequency ω_1. Despite the frequency changes, the cavity remains locked to the same resonance mode, leading to a shift in the center frequency of the laser. Frequency scans are typically conducted 2 to 4 times per day, with each scan lasting for approximately half an hour. During these scans, we record the center frequency of the crossover lines in the spectrum, as shown in Fig. 4.7. These measurements provide valuable data for analyzing

doi:10.6342/NTU202302912

and characterizing the frequency drift of the laser.

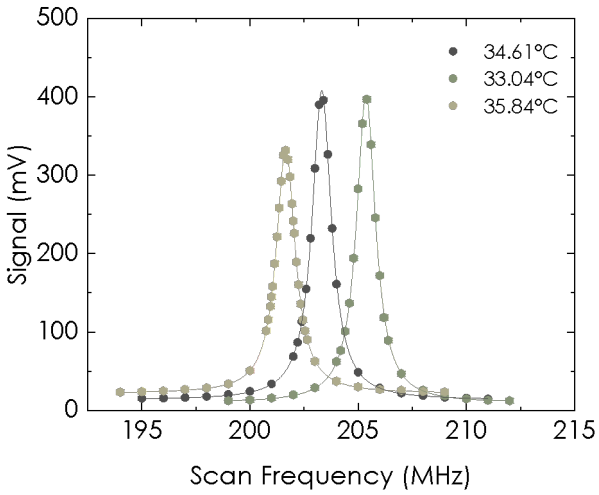

Figure 4.7: The peak frequency drift of the crossover line at different temperatures while scanning the frequency f_{EOM}.

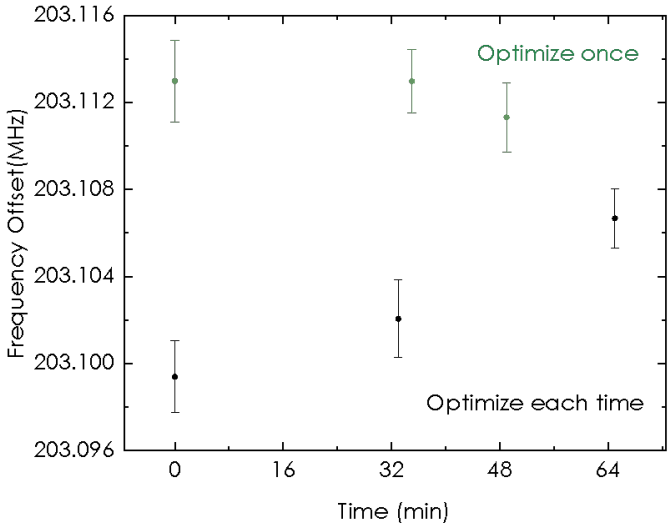

Figure 4.8: The peak frequency variation is analyzed to understand the central frequency error, which is attributed to the tilt angle of the probe and pump beams.

In order to optimize the power of the 459nm laser, the alignment of the optical path in the SHG laser system can be adjusted automatically. The probe and pump beam paths could slightly deviate from one another due to this optimization procedure. We made three measurements in one hour to analyze the impact of this optimization on the peak frequency of the Lamb dip, taking into account both the optimized and non-optimized

doi:10.6342/NTU202302912

conditions [23][25].

The pump and probe beams were overlapped over a distance of 54cm, and the spot variations were recorded using a CCD. Fig. 4.8 shows the measurement error, where in the non-optimized case, it was approximately 0.8 kHz. However, in the optimized case, with the alignment of the pump and probe beams having an uncertainty of around 1 μrad, the measurement uncertainty in the Lamb dip frequency was approximately 3 kHz [23].

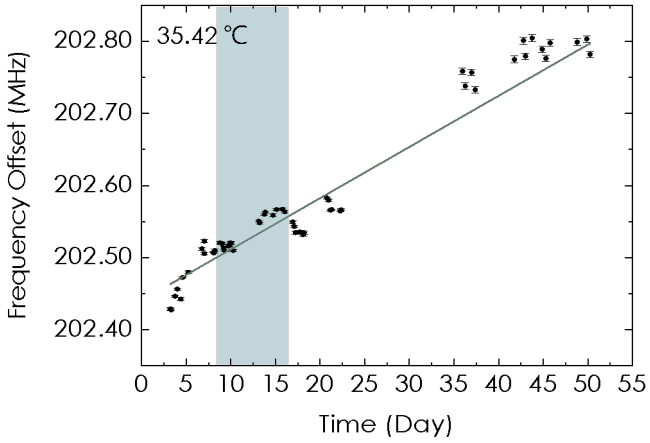

Figure 4.9: The long-term frequency drift is observed while the cavity is at 35.42°C. The shaded regions represent the periods during which the 1039nm laser is turned off to analyze the laser thermal shift.

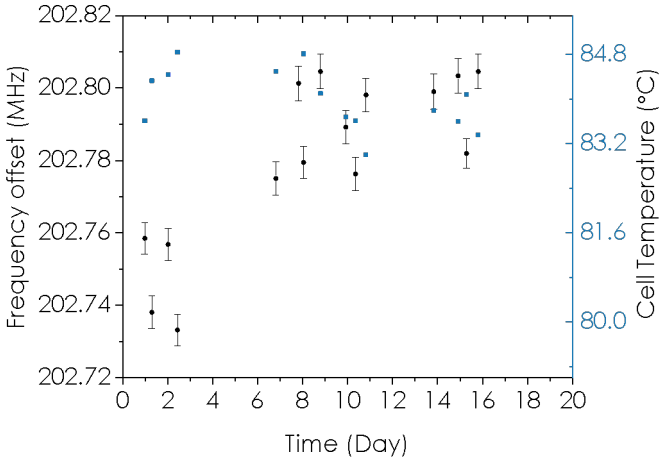

Figure 4.10: The frequency offset is compared with the Cs cell, considering temperature fluctuations, with the cavity temperature set at 35.42°C.

doi:10.6342/NTU202302912

During the experiment, it was observed that when the 1039nm laser is operated with an input power greater than 1mW, there is a frequency offset of approximately 20kHz between measurements taken with the laser turned off and measurements taken with the 1039nm laser on. This frequency offset is much larger than the variations observed during consecutive measurements. The shaded region in Fig. 4.9 represents the results of measurements taken over several days with the 1039nm laser turned off. It can be seen that the thermal effects caused by the laser accumulate over time and have a significant impact. Furthermore, the laser frequency is also influenced by the long-term temperature equilibrium. To mitigate these effects, the input power of the 1039nm laser has been reduced to below 1mW. As for the temperature fluctuations of the cell, as shown in Fig. 4.10, it is not significantly correlated with the measurement of the spectral lines in our system.

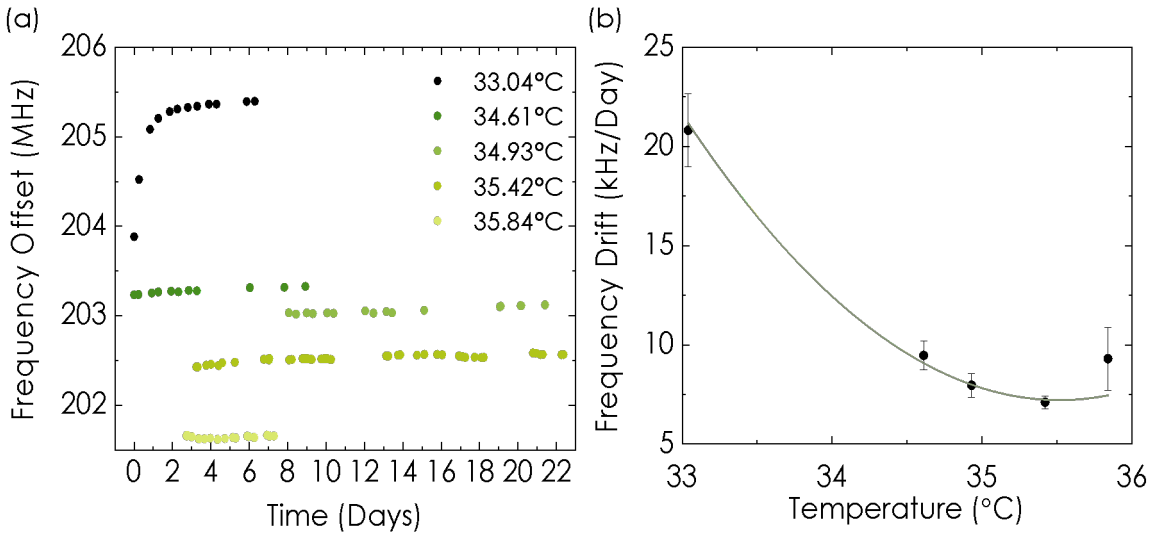

Figure 4.11: (a) The long-term frequency offset modulated by the fiber-EOM as indicated by the crossover signal. (b) The average frequency drift per day is measured while changing the temperature to find the zero-crossing temperature.

The discussion included the effects of the probe and pump beam alignment, laser power, and cell temperature on the measured spectral shift. The results of measuring multiple temperatures are presented in Fig. 4.11 (a). Based on the frequency shifts corresponding to each temperature, a plot is generated as shown in Fig. 4.11 (b), yielding a

doi:10.6342/NTU202302912

zero-crossing temperature of 35.56 ± 0.43°C. As of now, the temperature is maintained at 35.42°C, and over a period of approximately 50 days, the recorded frequency drift has shown an average of 7100.568 ± 322.633 Hz per day.

4.3 Rydberg Excitation

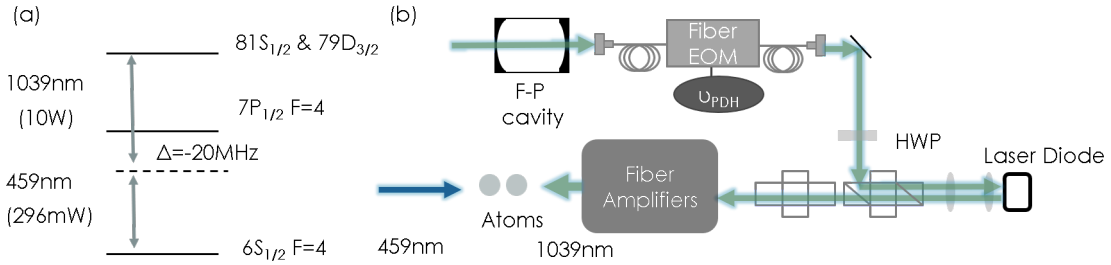

Figure 4.12: (a) The laser setup for two-photon Rydberg transition. (b) The lasers counter-propagate to the atoms.

When Rydberg atoms are generated in a magneto-optical trap (MOT), they can lead to fluorescence losses [26]. To determine whether the atoms are excited to the Rydberg state, we utilize the trap-loss spectroscopy technique [27]. We utilize stabilized 1039nm and 459nm lasers to excite atoms to specific Rydberg states, such as the $81S_{1/2}$ and $79D_{3/2}$ states. The energy difference between these two Rydberg states is approximately 6.2GHz.

In this experiment, the 1039nm laser is modulated using an EOM after passing through the F-P cavity. Subsequently, the modulated laser is injected into a laser diode locked to the +1 sideband of the EOM modulation. By adjusting the modulation frequency of the EOM, we can scan and control the frequency of the 1039nm laser.

During the frequency scanning process, our laser frequency is tuned by -20MHz from the transition of $6S_{1/2}$ F=4 to $7P_{1/2}$ F=4 as shown in Fig. 4.12. The scanning speed is approximately 1MHz/560ms. Throughout the scanning, the power of the 459nm laser is maintained at 296mW, while the power of the 1039nm laser is 10W.

doi:10.6342/NTU202302912

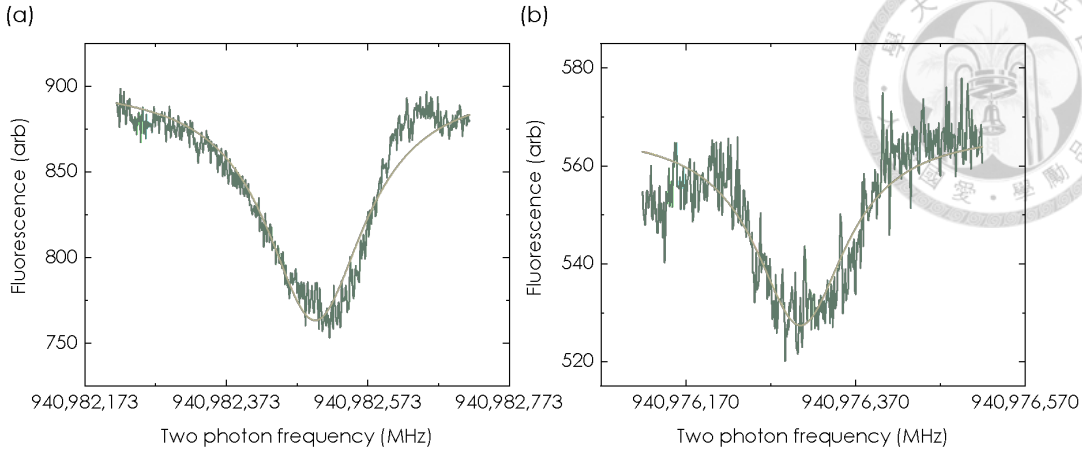

Figure 4.13: Trap-loss spectrum for cesium $6S_{1/2}$ F = 4 to (a) $81S_{1/2}$ and (b) $79D_{3/2}$ two photon Rydberg transition.

Rydberg states	Transition frequency (MHz)	FWHM(MHz)
$81S_{1/2}$	940982498	170.6
$79D_{3/2}$	940976305	130.7

Table 4.2: The transition frequency to the Rydberg state and the full width at half maximum (FWHM) of the linewidth by fitting the data with a Lorentian function.

Firstly, the 1039nm laser is turned on for 5 μs, followed by the simultaneous activation of the 459nm laser to drive the Rydberg state for 80 μs. During the last 30 μs, the CCD is activated to collect the fluorescence signal. We see the fluorescence trap-loss signal near the expected frequency. We observe the fluorescence trap-loss signal near the expected frequency, as shown in Fig. 4.13, and utilize Lorentzian function fitting the Rydberg transition frequencies and linewidths in Table 4.2.

doi:10.6342/NTU202302912

Chapter 5

Conclusion

In order to achieve high-fidelity two-qubit gates with Cs atoms, it is necessary to reduce the phase noise of the lasers and achieve narrow linewidths. To drive atoms into Rydberg states, we are using lasers with 459nm and 1039nm wavelengths to conduct two-photon excitations. However, in the case of the 459nm laser, which is the second harmonic laser, we utilize its master laser for frequency stabilization. Both lasers are locked to the cavity resonant frequency using the Pound-Drever-Hall (PDH) locking technique.

By generating an error signal with a high signal-to-noise ratio, we can provide feed-back to the current source and piezoelectric transducer (PZT) of the external-cavity diode laser (ECDL). This allows us to precisely lock both lasers to the resonant frequency of a high-finesse F-P cavity. The feedback bandwidth of the servo controller is carefully adjusted to maximize its effectiveness in suppressing laser phase noise.

To avoid servo bumps becoming a new source of noise for the atoms, we utilize the cavity as an optical filter. Through the DFM method, we accurately measure the cavity linewidth, which is much narrower than the servo bump frequency. We then utilize the

doi:10.6342/NTU202302912

transmitted light to perform injection locking on an additional laser diode, which serves as the seed for the fiber amplifier used to amplify the power of the 1039nm laser.

To determine the zero-crossing temperature of the ULE F-P cavity, we set up Doppler-free saturation spectroscopy as a frequency reference. This approach enables us to monitor the long-term frequency drift of the 918nm laser resonance within the cavity caused by temperature fluctuations. By setting the temperature near the zero-crossing temperature, we have been able to track the frequency drift over a period of 50 days. On average, the frequency drift amounts to 7kHz per day. Finally, we employ stabilized 1039nm and 459nm lasers to excite atoms to the $81S_{1/2}$ and $79D_{3/2}$ Rydberg states through trap-loss spectroscopy.

doi:10.6342/NTU202302912

References

[1] TM Graham, Y Song, J Scott, C Poole, L Phuttitarn, K Jooya, P Eichler, X Jiang, A Marra, B Grinkemeyer, et al. Multi-qubit entanglement and algorithms on a neutral-atom quantum computer. Nature, 604(7906):457–462, 2022.

[2] Dolev Bluvstein, Harry Levine, Giulia Semeghini, Tout T Wang, Sepehr Ebadi, Marcin Kalinowski, Alexander Keesling, Nishad Maskara, Hannes Pichler, Markus Greiner, et al. A quantum processor based on coherent transport of entangled atom arrays. Nature, 604(7906):451–456, 2022.

[3] Mark Saffman, Thad G Walker, and Klaus Mølmer. Quantum information with Rydberg atoms. Reviews of modern physics, 82(3):2313, 2010.

[4] Harry Levine, Alexander Keesling, Giulia Semeghini, Ahmed Omran, Tout T. Wang, Sepehr Ebadi, Hannes Bernien, Markus Greiner, Vladan Vuletić, Hannes Pichler, and Mikhail D. Lukin. Parallel implementation of high-fidelity multiqubit gates with neutral atoms. Phys. Rev. Lett., 123:170503, Oct 2019.

[5] Zhuo Fu, Peng Xu, Yuan Sun, Yang-Yang Liu, Xiao-Dong He, Xiao Li, Min Liu, Run-Bing Li, Jin Wang, Liang Liu, and Ming-Sheng Zhan. High-fidelity entanglement of neutral atoms via a Rydberg-mediated single-modulated-pulse controlled-phase gate. Phys. Rev. A, 105:042430, Apr 2022.

doi:10.6342/NTU202302912

[6] Sylvain de Léséleuc, Daniel Barredo, Vincent Lienhard, Antoine Browaeys, and Thierry Lahaye. Analysis of imperfections in the coherent optical excitation of single atoms to Rydberg states. Phys. Rev. A, 97:053803, May 2018.

[7] Harry Levine, Alexander Keesling, Ahmed Omran, Hannes Bernien, Sylvain Schwartz, Alexander S. Zibrov, Manuel Endres, Markus Greiner, Vladan Vuletić, and Mikhail D. Lukin. High-fidelity control and entanglement of Rydberg-atom qubits. Phys. Rev. Lett., 121:123603, Sep 2018.

[8] Lincoln David Turner, KP Weber, CJ Hawthorn, and Robert E Scholten. Frequency noise characterisation of narrow linewidth diode lasers. Optics communications, 201(4-6):391–397, 2002.

[9] Nur Ismail, Cristine Calil Kores, Dimitri Geskus, and Markus Pollnau. Fabry-pérot resonator: spectral line shapes, generic and related Airy distributions, linewidths, finesses, and performance at low or frequency-dependent reflectivity. Optics express, 24(15):16366–16389, 2016.

[10] Vittorio Degiorgio. Phase shift between the transmitted and the reflected optical fields of a semireflecting lossless mirror is π/2. American Journal of Physics, 48(1):81–81, 01 1980.

[11] Eric D Black. An introduction to pound–drever–hall laser frequency stabilization. American journal of physics, 69(1):79–87, 2001.

[12] J. I. Thorpe, K. Numata, and J. Livas. Laser frequency stabilization and control through offset sideband locking to optical cavities. Opt. Express, 16(20):15980–15990, Sep 2008.

doi:10.6342/NTU202302912

[13] Orazio Svelto, David C Hanna, et al. Principles of lasers, volume 1. Springer, 2010.

[14] Nitzan Akerman, Nir Navon, Shlomi Kotler, Yinnon Glickman, and Roee Ozeri. Universal gate-set for trapped-ion qubits using a narrow linewidth diode laser. New Journal of Physics, 17(11):113060, 2015.

[15] Lintao Li, William Huie, Neville Chen, Brian DeMarco, and Jacob P Covey. Active cancellation of servo-induced noise on stabilized lasers via feedforward. Physical Review Applied, 18(6):064005, 2022.

[16] Yang-Yang Liu, Zhuo Fu, Peng Xu, Xiao-Dong He, Jin Wang, and Ming-Sheng Zhan. Spectral filtering of dual lasers with a high-finesse length-tunable cavity for rubidium atom Rydberg excitation. Chinese Physics B, 30(7):074203, 2021.

[17] Jérôme Poirson, Fabien Bretenaker, Marc Vallet, and Albert Le Floch. Analytical and experimental study of ringing effects in a fabry–perot cavity. application to the measurement of high finesses. JOSA B, 14(11):2811–2817, 1997.

[18] RG DeVoe and RG Brewer. Laser-frequency division and stabilization. Physical Review A, 30(5):2827, 1984.

[19] N Uehara and K Ueda. Accurate measurement of ultralow loss in a high-finesse fabry-perot interferometer using the frequency response functions. Applied Physics B, 61:9–15, 1995.

[20] Hanne Ludvigsen, Mika Tossavainen, and Matti Kaivola. Laser linewidth measurements using self-homodyne detection with short delay. Optics Communications, 155(1):180–186, 1998.

[21] Jae Won Hahn, Yong Shim Yoo, Jae Yong Lee, Jae Wan Kim, and Hai-Woong Lee.

doi:10.6342/NTU202302912

Cavity ringdown spectroscopy with a continuous-wave laser: calculation of coupling efficiency and a new spectrometer design. Appl. Opt., 38(9):1859–1866, Mar 1999.

[22] Naoki Asuke, Nicolas Chauvet, André Röhm, Kazutaka Kanno, Atsushi Uchida, Tomoaki Niiyama, Satoshi Sunada, Ryoichi Horisaki, and Makoto Naruse. Analysis of temporal structure of laser chaos by allan variance. Physical Review E, 107(1):014211, 2023.

[23] C. Patterson, A. D. Vira, M. T. Herd, W. B. Hawkins, and W. D. Williams. Calibrating an ultra-low expansion cavity for high precision spectroscopy from 630 THz to 685 THz using molecular tellurium lines. Review of Scientific Instruments, 89(3):033107, 03 2018.

[24] WD Williams, MT Herd, and WB Hawkins. Spectroscopic study of the 7p1/2 and 7p3/2 states in cesium-133. Laser Physics Letters, 15(9):095702, 2018.

[25] Sang Eon Park, Ho Seong Lee, Taeg Yong Kwon, and Hyuck Cho. Dispersion-like signals in velocity-selective saturated-absorption spectroscopy. Optics Communications, 192(1):49–55, 2001.

[26] J. A. Aman, B. J. DeSalvo, F. B. Dunning, T. C. Killian, S. Yoshida, and J. Burgdörfer. Trap losses induced by near-resonant Rydberg dressing of cold atomic gases. Phys. Rev. A, 93:043425, Apr 2016.

[27] Jiandong Bai, Shuo Liu, Jieying Wang, Jun He, and Junmin Wang. Single-photon Rydberg excitation and trap-loss spectroscopy of cold cesium atoms in a magneto-optical trap by using of a 319-nm ultraviolet laser system. IEEE Journal of Selected Topics in Quantum Electronics, 26(3):1–6, 2020.

doi:10.6342/NTU202302912